Antifouling and stability enhancement of electrochemically modified reduced graphene oxide membranes for water desalination by forward osmosis

Mohamed Edokali [a], Mozhdeh Mehrabi [a], Oscar Cespedes [b], Chao Sun [a], Sean M. Collins [a,c], David Harbottle [a], Robert Menzel [c], Ali Hassanpour [a,*]

[a] School of Chemical and Process Engineering, Faculty of Engineering and Physical Science, University of Leeds, Leeds LS2 9JT, UK
[b] School of Physics and Astronomy, Faculty of Engineering and Physical Science, University of Leeds, Leeds LS2 9JT, UK
[c] School of Chemistry, Faculty of Engineering and Physical Science, University of Leeds, Leeds LS2 9JT, UK

ARTICLE INFO

ABSTRACT

In this study, an innovative electro-oxidative technique was employed to create graphene-based forward osmosis (FO) membranes. This involved constructing Polyethyleneimine crosslinked reduced graphene oxide (PEI:rGO) layers on scalable flat-sheet substrates functionalized with polyethylene glycol-Poly(3,4-ethylene-dioxythiophene)-poly (styrenesulfonate) (P:P:P) *via* electrophoretic deposition. Under the optimized electric potential of 10 V, we successfully combined PEI:rGO laminates with P:P:P support layers, resulting in a highly porous structure. The double-sided coated PEI:rGO membrane (DS-PEI:rGO) exhibited superior performance compared to the single-sided PEI:rGO membrane (SS-PEI:rGO). DS-PEI:rGO showed higher ion salt rejection (95 %) than that of SS-PEI:rGO (90.1 %) but slightly lower than the commercially-available Cellulose Triacetate (CTA-FO) membrane (99.3 %) in lab-scale FO desalination process. Interestingly, the resultant DS-PEI:rGO membrane exhibited reduced specific salt flux (0.014 g/L) compared to SS-PEI:rGO and CTA-FO membrane (0.017 g/L and 2.549 g/L, respectively). The antifouling properties of PEI:rGO membranes were assessed using synthetic seawater with sodium alginate. Under a 3.0 V DC potential, both PEI:rGO membranes experienced a 30 % increase in recovered flux compared to membranes without an electric field. This improvement was attributed to electro-oxidation mechanisms between PEI:rGO and oppositely charged ions, along with the unique nano-composite structure formed by PEI:rGO and P:P:P chains, contributing to enhanced membrane integrity.

1. Introduction

With increasing demand for low-energy consumption technologies for water treatment, forward osmosis (FO) has recently stood out as a breakthrough method for seawater desalination and wastewater treatment [1,2]. Compared to pressure- and thermally-driven membrane systems, FO is osmotically driven process by the chemical potential of draw solutes under no pressure requirement [3,4]. However, development of high-performance FO membranes is still the bottleneck for practical applications, and research efforts continue with the aim of

developing a new generation of FO membranes [5]. Commercial FO membranes still suffer from low antifouling properties and Internal concentration polarisation (ICP) issues, and their long-term performance can be also reduced by cleaning procedures during practical operations [6,7]. These identified challenges predominantly stem from the utilisation of a limited range of commercially-available polymeric membranes in the FO process, resulting in lowered water permeability and desalination efficiency [8,9]. Most recently, a few membrane suppliers have attempted to develop commercial polymeric FO membranes (*e.g.*, CTA) by altering their morphology which can improve water flux and minimise ICP effects. These improvements are found to be more suitable for wastewater treatment and impaired-aqueous feed solutions, however, such membranes still suffer from fouling and low water permeation for FO water desalination applications due to the low porosity and dense morphology [10–12]. Consequently, there exists a pressing requirement for the innovation and advancement of novel membrane materials to enhance the performance of FO, specifically tailored for water desalination purposes.

In recent years, the use of different nanotechnologies and nanomaterials has enabled the fabrication of novel and conductive FO membranes with high water permeability, salt rejection and anti-fouling performances [13–15]. As compared to commercially-accessible membranes, 2D graphene-based laminar membranes, including graphene oxide (GO) and reduced graphene oxide r(GO), have been receiving significant attention as promising candidates in water desalination and removal of organic molecules from water. Such laminar membranes can offer excellent ion selectivity by simply tuning interlaminar spacing between two adjacent GO sheets through reduction of GO or interaction with other cross-linkers and nanomaterials [6,16]. Different fabrication methods, including vacuum-assisted filtration, spin-coating, drop-casting, layer-by-layer (LBL), and electro-phoretic deposition (EPD), were employed to prepare layered GO-based FO membranes [17–20]. Nevertheless, construction of GO-based FO membranes under applied electrical potentials has been reported rarely [21]. This approach may open a new avenue for developing scalable membranes, particularly the fabrication of conductive GO-based FO membranes which can offer long-term desalination and stability performance, and better antifouling properties, outperforming the commercially-available FO polymeric membranes.

The reduction efficiency of graphene oxide (GO) using hydrophilic acids such as hydrobromic acid (HBr), hydroiodic acid (HI), sodium borohydride ($NaBH_4$) and hydrazine hydrate (HH) plays a crucial role in determining the properties of interest, particularly the electrical conductivity of the resulting reduced graphene oxide (rGO) films [21–24]. High electro-conductivity is of supreme importance in various applications, including reducing fouling through electro-oxidation processes in water-based treatment membranes [21,25]. Moreover, chemically modified graphene and its derivatives have shown promise in enhancing the dispersion of electrically conducting composites within polymeric or inorganic matrices, leading to numerous potential practical applications [21]. The synthetic methods of chemically modified GO significantly impact the performance and characteristics of rGO films, opening new possibilities for advanced materials for fabrication of newly developed water purification membranes using the FO process.

Lee et al., [26] successfully prepared polyethylenimine reduced graphene oxide (PEI:rGO) with an electrical conductivity of 492 S/m, significantly outperforming acid reduced graphene oxides. However, the electro-conductivity of polymeric-based reduced graphene oxides for preparation of conductive membranes still requires further investigation.

Over the last few years, there have been several research efforts to use conductive polymers for the preparation of water-based treatment membranes, especially for the prevention of fouling [27,28]. As such, poly (3, 4-ethylenedioxythiophene):poly(styrene sulfonate), with the chemical formula (PEDOT–PSS), is a type of conductive polymers which has controllable electrical conductivity, outstanding environmental

stability, and easy processability. PEDOT:PSS consists of two molecules of negatively charged PSS coating a conjugated and positively charged PEDOT polymer [29,30]. However, the electrical conductivity of pristine PEDOT:PSS is low as a result of PSS moieties, hence the practical demand for the production of highly conductive PEDOT:PSS thin films is still on-going for many industrial applications. Accordingly, many efforts have sought to increase electrical conductivity of such polymers by weakening the electrostatic interaction between anionic PSS and cationic PEDOT chains [31,32]. In this regard, various additives have been developed for doping with the PEDOT:PSS polymer to enhance its electrical conductivity, such as polar solvents and compounds, surfactants, acids, and poly-ethylene glycol (PEG) [33–35]. In addition, several researchers have reported improvements in the electrical conductivity of PEDOT:PSS through the incorporation of carbon-based nanomaterials as composites. These carbon nanomaterials have included carbon nanotubes (CNT) and graphene for electro-based practical applications, such as thermo-electric devices [36–38]. However, fabrication of rGO supported PEDOT:PSS films for water-based treatment by the concept of electrochemistry of conductive materials has not been reported yet. Such rGO composites present a further key route to develop a new generation of high-performance of laminar GO-based FO membranes for water desalination.

Advancements with the electrochemical oxidation processes for the prevention of organic foulants have been implemented with high efficiency in several water industrial applications [21,39–41]. Direct and indirect oxidation processes are responsible for hindering the accumulation of organic foulants through hydroxyl radicals and electron transfer between contaminants in water and the surface of anode under applied potentials [28]. In this regard, Rastgar et al., [40] have recently developed a novel electro-oxidative protocol to overcome the organic fouling in layered rGO-FO membranes. By imposing 2.0 V DC electrical potential on the surface of the prepared rGO membranes, the fouling behavior was significantly improved, resulting in 98.7 % of membrane flux recovery ratio. In addition, Liu et al., [42] have experimentally demonstrated an outstanding use of electro-chemical approaches to enhance the resistance to organic and microbial fouling of conducting carbon supported FO membranes under 2.0 V DC electrical potential applied in an electro-chemical cell. Despite the advances in the newly developed conductive membranes for anti-fouling behavior, the development of ideas and protocols for preparation of conductive FO membranes with highly balanced performance between anti-fouling ability and dimensional stability remains highly desirable and of substantial practical interest.

In this study, novel strategies are developed to fabricate conductive GO-based FO membranes by combing of as-synthesised PEI:rGO laminates onto the surface of conductively modified PEDOT:PSS support membranes using an EPD method under an optimized DC electrical potential. Herein, the synergistic utilisation of a conductive substrate composed of PEDOT:PSS/PEG with a conductive active layer, specifically tailored through chemical modification for the PEI:rGO membranes, illustrates an innovative approach, which to the best of our knowledge, has not been reported in the literature. This approach aims to resolve challenges associated with water permeation, anti-fouling properties, and stability concerns in FO-based desalination membranes. Furthermore, the fundamental principles of chemical modification applied to address these issues in FO-based membranes can also be extended and implemented within conducting membrane systems. Taking advantage of electro-conductivity of PEI:rGO nanostructures, the conductive membrane is synchronously prepared. Here, PEI:rGO laminates were stripped through an electrochemical exfoliation process, and that anodic-PEI:rGO was assembled onto the surface of cathode-PEDOT:PSS/PEG conductive substrate. The effect of the electrochemical process on the morphological and microstructural properties is further studied using different analytical techniques. Electrochemical properties of conductive membranes are also studied before and after fouling tests with the aid of surface electrochemical analyser. The performance and

stability of conductive PEI:rGO/ PEDOT:PSS/PEG - FO membranes are experimentally evaluated through comparison with the commercially available CTA-FO membrane and other GO conductive membranes reported in the literature. Moreover, the anti-fouling behavior of the resultant membranes is studied under and without DC electrical field in an FO desalination lab-scale system.

2. Experimental

2.1. Materials

As-synthesised branched polyethylenimine doped reduced Graphene Oxide (PEI: rGO-0.01) dispersion was prepared according to the procedure reported in section (SI-1, ESI 1) (*with 0.5 mg/mL GO concentration, stock GO dispersion from William Blythe Ltd, UK*). Commercial poly (3, 4-ethylenedioxythiophene)-poly (styrenesulfonate) (*PEDOT: PSS, 3.0–4.0 % in H_2O, high-conductivity grade, > 200 S/cm, pH 1.5–2.5*), N-methyl-2-pyrrolidone (*NMP, 99 % pure*), N, N-Dimethylformamide (*DMF, 99.9 %, anhydrous*), sodium Alginate (*SA*), and polyethylene glycol (*PEG 400, Mw = 400 g.mol^{-1}*) were purchased from sigma-aldrich (UK). 4-methyl piperidine (4-MP) was provided by Fluorochem Limited. Non-Woven Fabric (*NWF, soft and pure Polypropylene Material, 375* μm *Thick*) was obtained from EasyMerchant Limited (UK). Sodium chloride (*NaCl*, M.W: 58.44 g/mol) was provided by VWR International Ltd. Dextrose ($C_6H_{12}O_6$, M.W: 180.16 g/mol), calcium chloride (*CaCl$_2$*, M.W: 110.98 g/mol), and sodium sulfate (*Na$_2$SO$_4$*, M.W: 142.04 g/mol) were purchased from Alfa Aesar. Commercial FTSH2O Cellulose Triacetate flat-sheet (porosity:~ 70 %, thickness:~ 50 μm) membranes were purchased from STERLITECH corporation. Ethanol (*CH$_3$CH$_2$OH*, ≥ 70 % v/v) and sodium hypochlorite (*NaOCl*, ≥ 10 % chlorine, M.W: 74.44 g/mol) were provided by Scientific Laboratory Supplies (SLS). Deionised (DI) water (*18.2 MΩ-cm*) from an ultrapure water purification system was used throughout this work.

2.2. Methods

2.2.1. Membrane fabrication

2.2.1.1. Fabrication of P:P:P scalable support layers. The as-prepared support membrane (*denoted as P:P:P*) was prepared by casting through non-solvent induced phase separation (NIPS) at ambient temperature [43]. Here, the fabrication process of the conductive substrates was explained based on the controlled amounts of additive materials, as shown in Fig. 1 and Fig. SI-2. It is worth mentioning that our initial membrane preparation efforts to prepare homogenous and stable mixtures of doped conducting polymer with no PEG-400 were unsuccessful, showing fracture on the surface of the cast PEDOT:PSS layer after drying the support membranes. Hence, DMF/NMP (25 wt%) was simultaneously mixed with 4-MP (12 wt%, as a gelation inhibitor to the mixture) and PEG-400 (3 wt%, as stability and conductivity enhancement agent to the additive polymer) for 5 min. PEDOT: PSS conducting polymer (60 wt%) was then added dropwise to the mixture over 10 min. The whole mixture was kept stirring at 350 rpm at room temperature for 48 h to prepare a homogenous solution. Then, the solution was heated in a water bath at 45 °C for 8 h under continuous and constant stirring in a sealed beaker to swell the polymer mixture and ensure the polymer was completely dissolved. Subsequently, the obtained polymer solution was kept in a vacuum oven at 40 °C for 4 h to completely remove any air bubbles.

The synthesised PEDOT:PSS/PEG solution was cast on a non-woven fabric fitted onto the top of a hydrophobic surface that was held by scotch tape on flat glass sheet, using a micrometer adjustable applicator (BGD 209/2S, Biuged). The resultant membrane (*denoted SS-P:P:P*) was then dried for 4 h at room temperature, and then another layer of doped
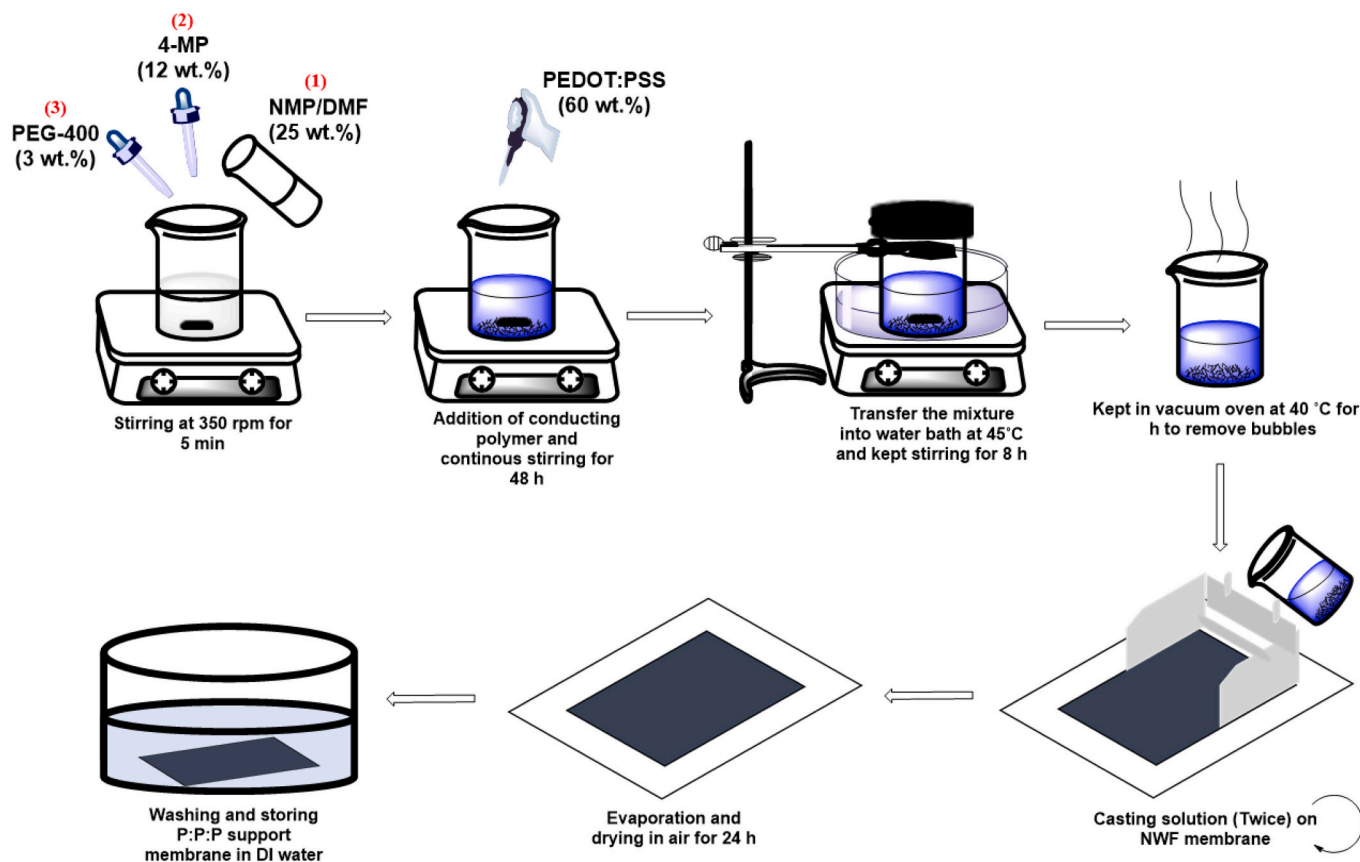

Fig. 1. Schematic illustration of the preparation protocol for the conductive P:P:P support membrane.

polymer was cast again and dried for 24 h. After drying, the membranes were immersed and rinsed several times with a fresh DI water over 12 h to remove any excess of contaminates. The obtained membrane was kept in a DI water and stored inside a sealed chamber at 25 °C for further use. For performance comparison, another conducting substrate was prepared by coating the doped polymer mixture similarly on both sides of the non-woven. This resultant support layer was denoted as (*DS-P:P:P*) membrane.

2.2.1.2. Electrochemical preparation of conductive (P:P:P/PEI:rGO) membranes. Electrochemically conductive membranes were fabricated by electrophoretic deposition in a crystallising dish (9.5 cm diameter, 5.5 cm height). A titanium (Ti) plate (with maximum DC potential of 25 V; size of 7.0×3.0 cm^2) was horizontally fitted at the base of the dish and used as an anode. The as-prepared P:P:P support membranes (size of 5.5×5.1 cm^2) was used as a cathode and placed perpendicular to the Ti plate using membrane holder in-house built (prepared using highly conductive copper wires, as shown in Fig. SI-3), with an adjusted distance of approximately 1.0 cm between the cathode and anode. The crystallising dish was filled with the as-synthesised PEI:rGO dispersion to a height approaching 1.0 cm from the base. Using an electrical power supply, an optimized DC voltage of 10 V was applied between the Ti cathode and the P:P:P flat-sheet anode as shown in Fig. 2 and Fig. SI-4 [see supplementary video for electrochemical reaction and assembly – ESI 2]. After an optimum coating time of 7 h, the PEI:rGO dispersion started to bubble and expand, and simultaneously PEI:rGO sheets began to strip-off from the water dispersible mixture and assemble on the

surface of P:P:P support membranes by electrophoresis process. The obtained conductive membrane (*denoted as SS-PEI:rGO*) was dried and stored in a desiccator for later use. For comparison, a double-sided conductive membrane (*denoted as DS-PEI:rGO*) was also prepared by assembling PEI:rGO laminates through applying the same EPD voltage on both sides of the P:P:P support membrane. Modelled structures of the commercial NWF and prepared P:P:P substrates and PEI:rGO membranes are shown in Table 1. The resultant membranes which were fabricated by both casting and EPD methods, are presented in Fig. SI-5, ESI 1.

2.3. Characterisations

2.3.1. Zeta potential (ZP)
The zeta potential of PEI-doped rGO dispersions was measured at various time intervals using a Zetasizer Nano ZSP ZEN5600 (Malvern Panalytical, UK). The equilibration time was set to 120 s, and the measurements were conducted at ambient temperature using the auto processing mode. Prior to the ZP measurements, dispersion samples were prepared by optimizing their dilution factor by 5×. Measurements were repeatedly taken to ensure the stability of ZP surface charges.

2.3.2. Fourier transform infrared (FTIR) spectroscopy
Membrane samples were subjected to Fourier Transform Infrared (FT-IR) spectroscopy using a NICOLET iS10 equipped with a diamond Attenuated Total Reflectance (ATR) accessory from Thermo Fisher. The measurements were performed in transmission mode, covering a
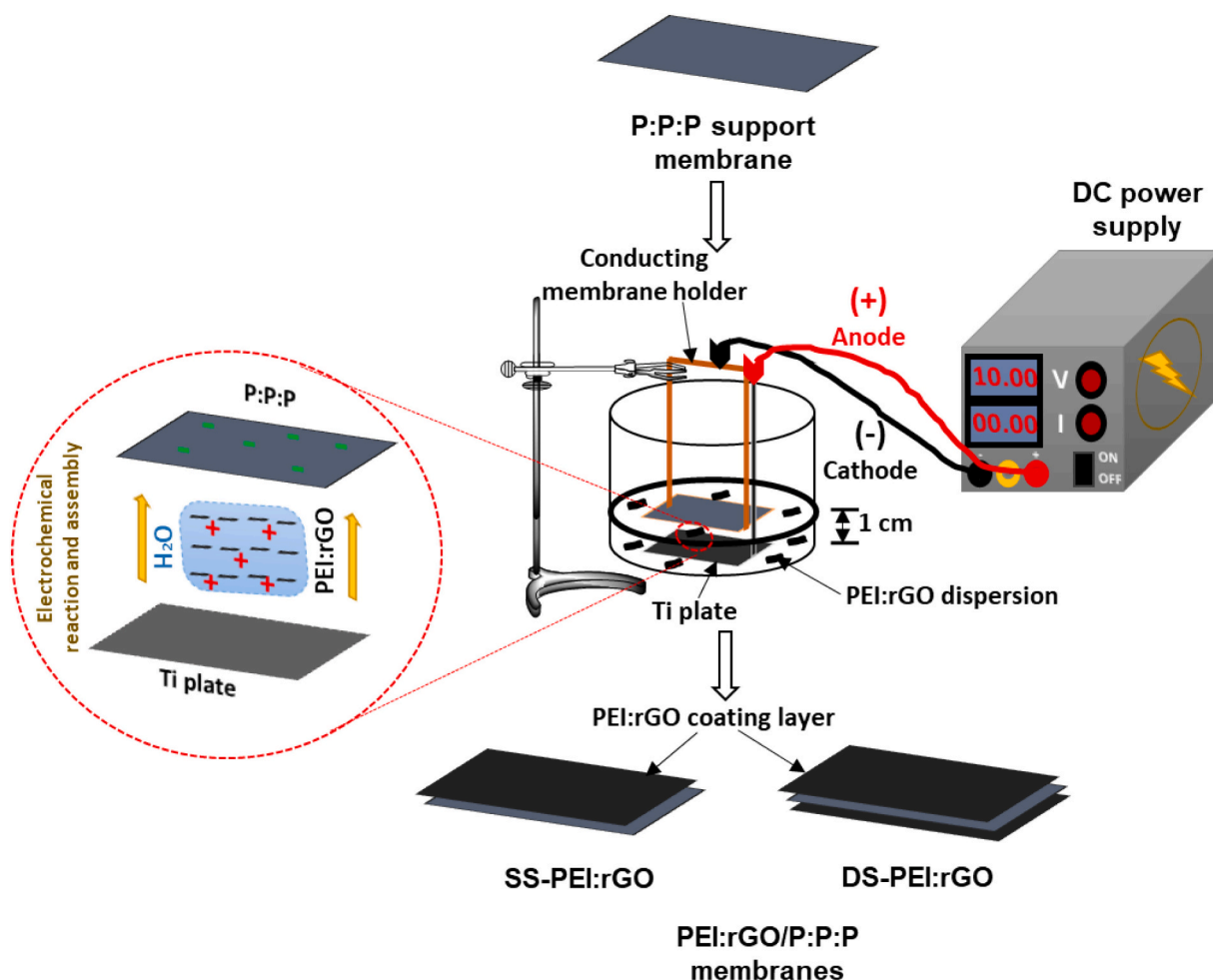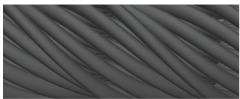
Fig. 2. Schematic presentation of the fabrication scheme of SS- and DS-PEI:rGO conductive membranes using the in-house built electrochemical EPD setup, including illustration of intercalation and assembly of PEI:rGO laminates by electro-conductivity interactions on surface of P:P:P conductive substrates.

Table 1
Configurational structures of commercial NWF, P:P:P substrates, and PEI:rGO (EPD) membranes.

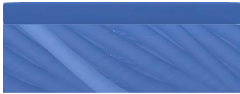| Sample	Modelled structure
NWF	Pristine NWF Film
SS-P:P:P	Single P:P:P layer / P:P:P-coated NWF
DS-P:P:P	1st P:P:P layer / P:P:P-coated NWF / 2nd P:P:P layer
SS-PEI:rGO	Single PEI:rGO laminates / Single P:P:P layer / P:P:P-coated NWF
DS-PEI:rGO	1st PEI:rGO laminates / 1st P:P:P layer / P:P:P-coated NWF / 2nd P:P:P layer / 2nd PEI:rGO laminates

wavelength range of 525 to 4000 cm^{-1}. Each sample underwent 64 scans, and the spectral resolution was set at 4 cm^{-1}.

2.3.3. Raman spectroscopy

The Raman spectra of the membranes were acquired using a HORIBA JOBIN YVON LabRAM HR 800 Raman Microscope with a 600 ln/mm grating. The measurements were carried out with a 50 times magnification, employing a 532 nm laser. The Raman shift range explored ranged from 500 to 2500 cm^{-1}. To ensure the quality of the data, several steps were taken. First, a baseline subtraction was performed to enhance the signal-to-noise ratio. The data acquisition parameters were optimized for accurate and reliable results. Each sample was exposed for 600 s, with a laser power of approximately 10 mW. To improve the signal robustness, three accumulations were performed for each sample, enhancing the statistical significance of the measurements.

2.3.4. X-ray diffractometer (XRD)

X-ray Diffraction (XRD) analysis was conducted using a Bruker D2 X-ray diffractometer equipped with a Cu-K (α) radiation source (wavelength, λ = 1.5418 Å). The X-ray diffractometer was operated at a constant voltage of 30 kV and current of 10 mA. Each XRD scan lasted for 20 min, during which the sample was rotated at a speed of 30° per minute. The XRD measurements covered a 2θ angle range from 5° to 80°, with a step size resolution of 0.02°, and each step took approximately 41.3 s.

2.3.5. Surface morphology

Field emission scanning electron microscopy (FE-SEM) using an SU8230 Hitachi instrument, in conjunction with energy dispersive X-ray spectroscopy (EDX) from OXFORD instruments, was employed to comprehensively analyse the surface characteristics, cross-sectional profiles, and surface chemical compositions of the membrane specimens. In advance of SEM imaging, all samples were meticulously mounted onto specialized aluminum SEM stubs, followed by a carbon coating process utilizing an ion sputtering device for a duration of 3 min. FE-SEM images were acquired utilizing the normal lens mode, with

operational parameters set at an accelerating voltage of 2.0 kV and an optimal working distance of 8.0 mm. For EDX investigations, a high lens mode was utilized, and data were collected at an accelerating voltage and working distance of 15.0 kV and 15.0 mm, respectively.

The surface topography of the membranes was analyzed using a Bruker - NPFlex Surface 3D Optical Profilometer. This technique quantified the surface roughness in terms of the average roughness (R_a). The measurements were carried out in a non-contact mode with a scanning rate of 25 min per scan. The instrument used a $10\times$ objective and scanned an area of 5.0 mm $\times$ 5.0 mm.

2.3.6. Water contact angle (WCA)

The wettability of the surface membrane was evaluated using the sessile droplet method using a KVS optical tensiometer (KSV CAM 200). To assess wettability, a 1.58 μL droplet of deionised (DI) water was carefully positioned on the membrane surface. The contact angles were measured and averaged using the 'Attension Theta' software. To ensure reliability, each measurement was performed three times at different positions on the membrane, allowing good assessment for the stability of droplets and the consistency of the results.

2.3.7. Electrochemical properties of membranes

The electrochemical impedance spectroscopy (EIS) of the membranes was conducted using a four-point probe method on an interface 1010ETM Potentiostat workstation (Gamry instruments Inc.) within a Memmert HCP150 humidity chamber at a temperature of 25 °C. Prior to measurement, the membrane samples were cut into dimensions of 3.0 cm $\times$ 1.0 cm. The samples were then placed in a BekkTech BT-110 conductivity clamp, consisting of a Teflon case with two current electrodes and two potential-sensing electrodes, spaced apart from each other (refer to Fig. SI-6, ESI 1). To enhance conductivity, the membrane samples were fully immersed in DI water. The potentiostatic EIS measurement parameters were configured as follows: initial frequency (10,000 Hz), final frequency (0.1 Hz), AC voltage (10 mV rms), and estimated resistance (Z) of 10 Ω. To ensure accuracy and reliability, the EIS measurements were repeated five times for each sample, both before and after anti-fouling tests. From the EIS measurements, the conductivity (**k, S/m**) of membranes was theoretically determined as follows [27]:

$$k = \frac{L}{RWd} \tag{1}$$

where (**R**) is resistivity of membranes (in **Ohms**). (**L**) is the distance between two coupling electrodes (in **m**), (**W**) and (**d**) are measured width and thickness of the membrane (in **m**), respectively.

2.4. Evaluation of membrane performance in an FO system

Forward osmosis experiments were conducted using lab-scale systems shown in Scheme (SI-2, ESI 1). The FO membrane cell which holds the membrane with an effective area of 6.16 cm^2, separates feed and draw solutions tanks. For FO desalination test, 0.1 M NaCl (aqueous) and 0.5 M dextrose (aqueous) were used as feed and draw solutions, respectively. The solutions were hydraulically circulated using a gear pump at room temperature with an optimum flow rate of 200 mL/min for 6 h. Water flux (**Jw**, $L \cdot m^{-2} \cdot h^{-1}$, **LMH**) and salt rejection (**R, %**) across the membranes was determined using the following Eq. [44]:

$$J_w = \frac{\Delta V}{A \cdot \Delta t} \tag{2}$$

$$R = \left(1 - \frac{C_p}{C_f}\right) \times 100 \tag{3}$$

where (**Δ V**) is the measure of volume changes of the feed solution (**in L**) across the membrane active area (**A in m^2**) at the interval time (**Δ t in h**).

(C_p) and (C_f) represent permeate salt and initial feed salt concentrations, determined by the change in the total dissolved solid (TDS), respectively.

For determination of ICP effects, the reverse salt ions were determined using the same FO system, with DI water and 0.6 M NaCl aqueous solution used as feed and draw solutions, respectively. The revere solute flux (**RSF, J_s, $g\cdot m^{-2}\cdot h^{-1}$, gMH**) was calculated as follows [13]:

$$J_s = \frac{\Delta(C_t V_t)}{A.\Delta t} \quad (4)$$

where (C_t in g/L) and (**V** in L) denote the change in salt concentration and volume of the feed solution across the effective area of membrane (**A**) at an interval time (**Δt**). Moreover, the specific salt flux (J_{sp}, g/L) of membranes was determined as the ratio of the RSF to the water flux using [45–47]:

$$J_{sp} = \frac{J_s}{J_w} \quad (5)$$

Intrinsic separation properties of membranes, including the pure water permeability coefficient (**A**), the salt permeability coefficient (**B**), the porosity (**ε**), the structural parameter (**S**) and tortuosity (**τ**), were assessed according to the data obtained from the four-stage theory as illustrated in Section (S2, SI).

2.5. Membrane fouling test procedure

Anti-fouling properties of the resultant membranes were determined by conducting fouling experiments in the same FO process, under both zero voltage and applied electrical field, as shown in Fig. SI-7, ESI 1. The procedure is adopted from literature [40,48] and slightly modified to fit the capability of our FO lab-scale rig. Initially, a feed solution, containing 1 mM of CaCl$_2$ and 10 mM of Na$_2$SO$_4$, and 1 M of NaCl as a draw solution were counter-currently circulated in the FO lab-scale process. After flow stabilisation for 80 min, SA (1000 ppm) as an organic foulant was added dropwise into the above feed solution to start the fouling tests. Each fouling experiment was performed in two cycles of 8 h, (16 h in total), with a crossflow rate of 8.5 cm/s at room temperature. To assess the fouling reversibility after each cycle, the membrane was then exposed to hydraulic backwashing at high crossflow (1236 mL/min) for 30 min using a DI water on both sides of membrane surface. The flux recovery ratio (**FRR, %**) and total flux decline ratio (**R_t, %**) were calculated using [40,48]:

$$FRR = \frac{J_R}{J_0} \times 100 \quad (6)$$

$$R_t = \frac{J_0 - J_{steady}}{J_0} \times 100 \quad (7)$$

where J_R (**LMH**) denotes the recovery flux after backwashing of membrane, J_0 (**LMH**) represents the initial water flux, and J_{steady} (**LMH**) indicates the steady water flux obtained during fouling tests.

The anti-fouling behavior of the membranes were assessed under an optimized electrical potential of 3.0 V applied on the surface of the membrane using a direct current (DC) power supply (LOGNWEI® 30 V, 10 A). Using two pieces of copper tape, one point on the membrane surface was connected to a cathode and another point was connected to a stainless-steel sheet as an anode with a fixed distance of approximately 0.3 cm, as shown in Fig. SI-8, ESI 1.

2.6. Structural stability tests

The chemical stability and durability of membranes were qualitatively evaluated by soaking in aqueous solutions of NaCl (*with a concentration 0.6 M*) and NaClO (*with different concentrations of 1000, 10,000, and 30,000 ppm*). Prior to the experiments, the samples were cut into small strips and structural durability of each membrane was periodically monitored.

The mechanical strength of membranes was determined by conducting tensile testing and structural integrity testing on harsh environmental conditions. The tensile test on membranes was performed using a universal testing machine (Instron Model 5566) with a tension speed rate of (2.0 mm/min) and maximum load of 2.5 N. Prior to the measurements, the samples were prepared by cutting into strips of 0.5 cm × 5.0 cm. On the other hand, the structural integrity test was also conducted by simply ultra-sonicating the membrane samples (size cut of 2.0 cm × 2.5 cm) in a water bath and qualitatively monitoring their stability as a function of time.

3. Results and discussion

3.1. Deposition mechanism of PEI:rGO laminates on P:P:P support layer

After successful preparation of P:P:P support layers, the PEI:rGO laminates were carefully applied onto the surface of P:P:P substrates using the EPD technique, employing an optimal voltage of 10 V over three different durations: 4, 7, and 10 h. During the DC voltage application, the edge sites and grain boundaries of the PEI:rGO anode underwent oxidation, leading to the expansion of the modified rGO layers [49]. Simultaneously, the water electrolysis process generated hydroxyl radical anions, which were incorporated into the expanded PEI:rGO, while oxygen resulting from water ionization entered the PEI:rGO layer [49,50]. This action caused the dissociation of the PEI:rGO dispersion, and subsequently, PEI:rGO laminates were separated from the water dispersible solution. Guided by the electric field, the formed PEI:rGO sheets moved towards the cathode and assembled on the surface of the P:P:P substrate, as demonstrated in the supplementary video (SI - ESI 2). Notably, the positively charged PEI:rGO was attributed to the protonation of carboxyl groups at the edges of GO flakes, interacting with the positive charges from PEI [51]. Furthermore, it was observed that the electronegativity of PEI:rGO laminates towards the P:P:P substrate increased for the freshly synthesised PEI:rGO dispersion with higher ZP value (higher pH 7.4), compared to that of one-week old which has lower ZP value and accordingly reduced pH (pH 3.9), (refer to Fig. SI-9, ESI 1). This phenomenon could describe the progressive degradation of amine groups for the PEI:rGO dispersion over a period, elucidating the rationale behind the suboptimal performance of the one-week-old sample in the process of membrane fabrication. The electrophoretic process allowed the deposition of PEI:rGO laminates onto the cathode P:P:P flat-sheet substrate, exploiting the electric field force, as depicted in Fig. 2. The significance of zeta potential in the electrophoretic deposition of membranes was also noted. In essence, the electrophoretic mobility of particles directly correlated with their zeta potential, emphasizing the importance of zeta potential in determining deposition efficiency [52]. Notably, the higher zeta potential value of the synthesised PEI:rGO dispersion made it more suitable for electrophilic membrane deposition compared to dispersions with lower zeta potentials (refer to Fig. SI-9, ESI 1).

3.2. Membrane morphology characterization

Fig. 3.a depicts the SEM images of showing the surface morphology of both the P:P:P support layers and PEI:rGO-based membranes, fabricated through NIPS and EPD techniques, respectively. For the P:P:P support layers, as shown in Fig. 3.a-i and -ii, the coated membrane displays a smooth and uniform PEDO:PSS/PEG coating. However, the presence of NWF fibers is still evident on the surface of the coated layers. The cross-sectional SEM images Fig. S10.a and b of SS- and DS-P:P:P layers reveal that the membrane comprises nanofiber layers with a thickness of approximately 378 ± 18.9 μm and 381 ± 19.3 μm, respectively. These underlying nanofibers exhibit high porosity throughout the membranes microstructure, facilitating maximum

(a)
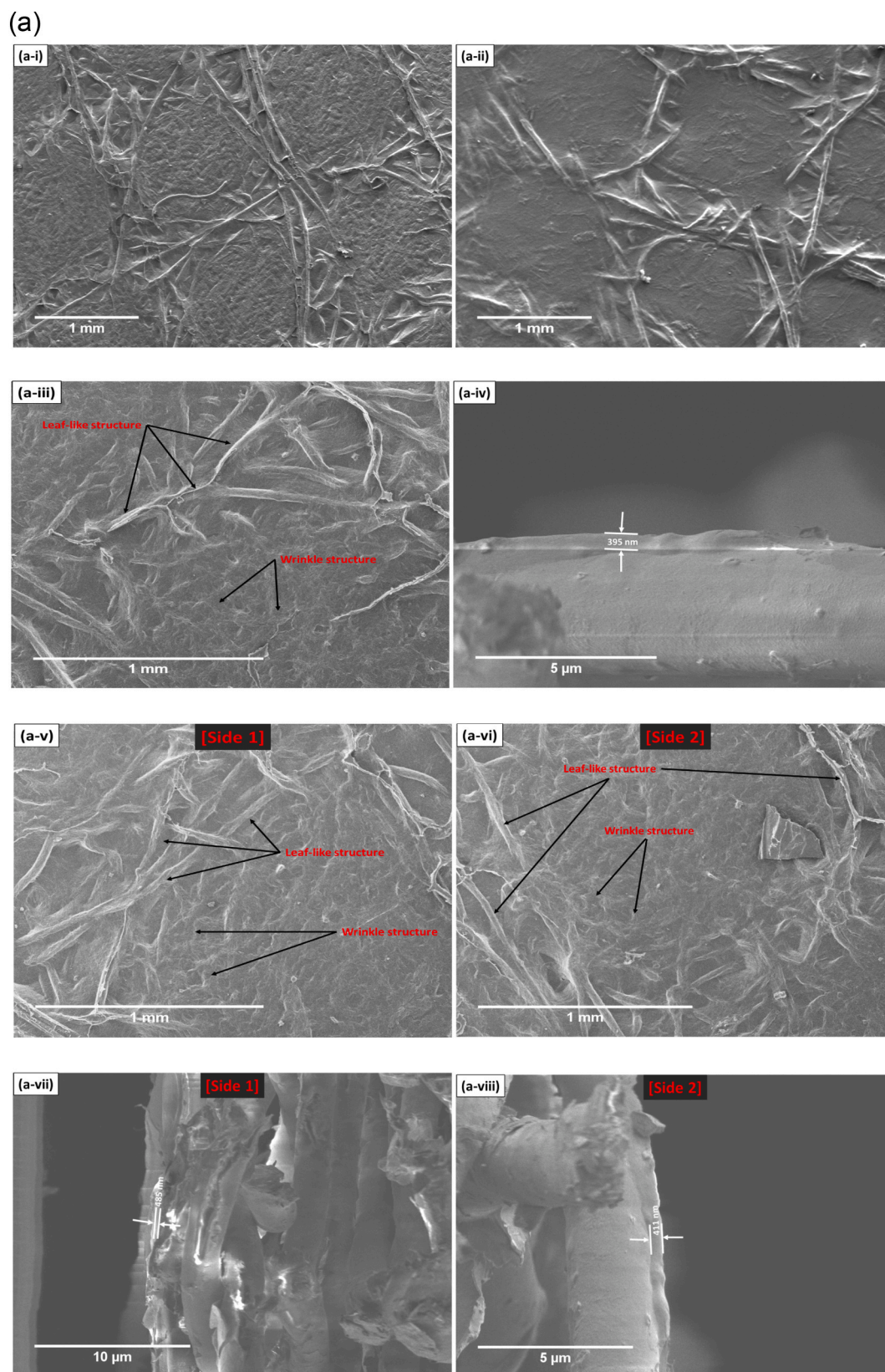
Fig. 3. (a) FE-SEM surface morphology and cross-sections, **(b)** average surface roughness and **(c)** dynamic contact angle measurements of conductive P:P:P and PEI: rGO membranes, compared to the commercial NWF film.
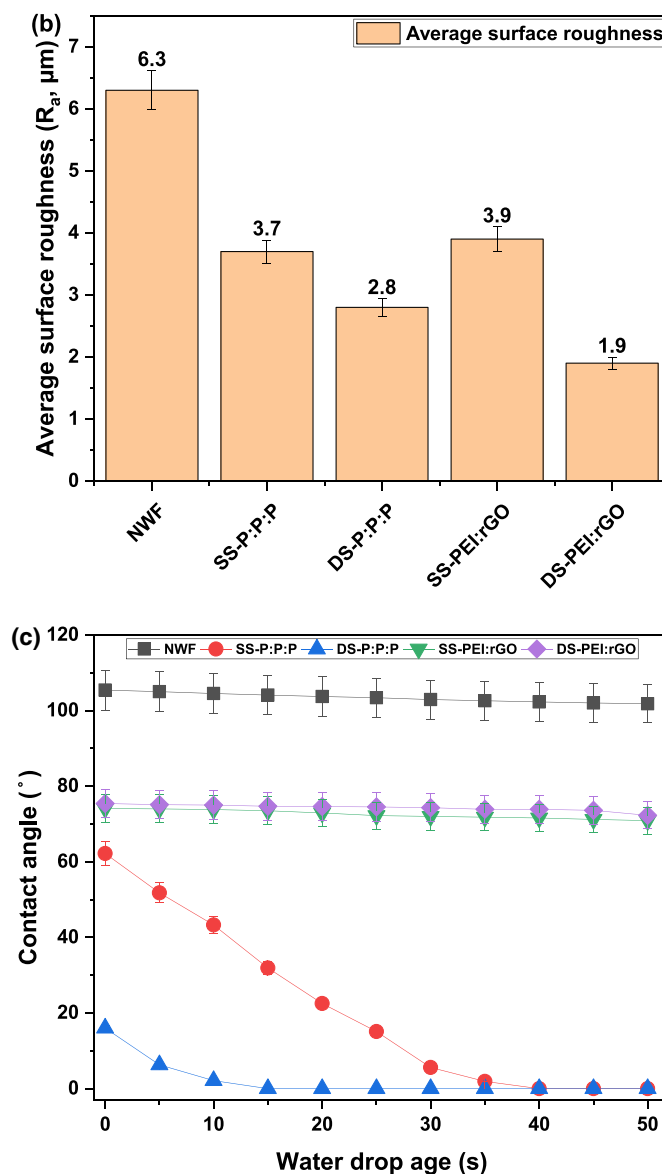
Fig. 3. (*continued*).

contact between the P:P:P layers and the draw solution during FO operations. This feature leads to a higher mass transfer area and, consequently, increased water flux [53,54]. On the other hand, (Fig. 3.a-iii, -v, and -vi) demonstrate the surface morphology of the SS- and DS-PEI:rGO membranes. Notably, the PEI:rGO selective layer was successfully formed on the P:P:P support sheets. The SEM images after EPD deposition reveal a leaf-like structure with typically undulating and wrinkled features, unlike the nanofibrous matrix observed in the P:P:P support layers. These typical wrinkles are attributed to the stacked PEI:GO boundaries, which serve as both water permeability enhancers and spaces for enhancing mechanical strength [20,48]. Furthermore, attempts were made to determine the thickness of the deposited PEI:rGO laminates, as shown in Fig. 3.a-iv, vii, and viii and Fig. SI-10.a and b, ESI 1. The SS-PEI:rGO membrane exhibited a PEI:rGO laminate thickness of (395 ± 13.6 nm), while the DS-PEI:rGO membrane demonstrated double-side laminates with thicknesses of (485 ± 21.2 nm) and (411 ± 18.6 nm), respectively. Characterizing the cross-sections of deposited PEI:rGO laminates proved to be challenging, but SEM analysis provided valuable insights into their thickness.

Surface NPFlex characterization plays a critical role in understanding the overall surface topology on a larger scale, particularly the surface

roughness of membranes. This knowledge is of utmost importance in controlling the antifouling behavior of the membrane [55]. In Fig. 3.b and Fig. SI-13, ESI 1, the average surface roughness measurements and corresponding 2D and 3D NPFlex images of the as-prepared membranes were summarised and depicted, respectively. An interesting observation is that the introduction of PEDOT:PSS/PEG casting leads to a reduction in the average surface roughness of the NWF (nano-fibrous) membranes. This decrease is attributed to a diminishing electrostatic interaction between PEDOT and PSS [34]. Furthermore, the addition of PEG further contributed to reduce the surface roughness in the PEDOT:PSS polymer backbone [34,56,57]. The topographic images of the P:P:P (PEDOT:PSS/PEG) membranes reveal a uniform ridge-and-valley morphology, which is characteristic of membranes formed through the NIPS method [27]. However, after coating these membranes with PEI:rGO laminates using EPD, a noticeable improvement in smoothness is observed. This enhancement is attributed to the presence of randomly dispersed PEI:rGO on the P:P:P membrane surface, effectively covering substrate defects due to the PEI crosslinked rGO laminates [58–61]. It is noteworthy that the average roughness (R_a) of the resulting PEI:rGO membranes is substantially decreased compared to the P:P:P membranes. This reduction in roughness proves to be highly beneficial as it helps mitigate

fouling propensity on the membrane surface.

The WCA analysis reveals the wettability of the membrane surface, a critical aspect affecting filtration performance and membrane fouling [61]. In osmotically driven membrane processes, the wettability of the membrane surface is crucial to performance. This is because solutes can diffuse exclusively within the wetted area of the support sheet, while the unsaturated parts within the internal structure of the support layer cannot be considered as actual mass transfer areas [62]. Fig. 3.c and Fig. SI-14, ESI 1 illustrate the changing of WCA of NWF, P:P:P, and PEI:rGO-based membranes. After applying PEDOT:PSS/PEG on P:P:P-coated membranes, the water contact angles were observed to be lower compared to pristine NWF. This improvement is attributed to the presence of the sulfonic group (SO$_3$H) and amine group (−NH$_2$) from PSS and PEG, respectively [56,63,64]. These functional groups enhance the surface energy and polarity of the membranes, making them more hydrophilic, and hence resulting in higher water flux. The content of PEDOT:PSS/PEG was found to be the most influential factor in enhancing the membranes wettability. On the other hand, the contact angles for PEI:rGO-based membranes increased due to the partial removal of functional groups (carboxyl, epoxy, and hydroxyl groups) [61]. Despite this, the membranes still retained some GO content and amine groups, as indicated by contact angles <90° [46,61]. These membranes with such WCA angles appear to be well-suited for FO water applications.

3.3. Membrane physico-chemical analysis

The investigation of the chemical structures of P:P:P and PEI:rGO/P:P:P membranes was firstly conducted using FT-IR spectroscopy, as depicted in Fig. 4.a. In the FTIR spectrum of the P:P:P film, the presence of peaks at 2873 cm^{-1} (C—H stretching) and 1710 cm^{-1} (C—O—H bending) confirms the presence of PEG in the film and on the surface of the fabric. Additionally, peaks at around 1320, 1110, and 485 cm^{-1} indicate C=O stretching from the ether linkage of PEG, and a broad peak at 3490 cm^{-1} corresponds to —OH stretching. The spectrum also confirms the presence of S—O sulfonyl stretching group (sulfur bonds) and C—C stretching from the PEDOT:PSS at prominent peaks around 1255 cm^{-1} and 1471 cm^{-1}, respectively [34,57,65,66]. After coating the P:P:P film with PEI:rGO laminates, new peaks are observed at 1480.7 cm^{-1}, suggesting the presence of carboxyl and carbonyl functional groups. Additionally, peaks at 3241.6 cm^{-1}, 1584 cm^{-1} and 610.3 cm^{-1} indicate the incorporation of nitrogen-containing amine groups through PEI molecules, confirming the successful integration of these groups on the surface of PEI:rGO-based membranes [26,58,61,67].

In the context of the hybrid P:P:P thin film, the interaction between PEDOT and PSS within the polymer matrix is primarily driven by the Coulombic force of attraction [68]. The introduction of PEG serves as a screening agent, enhancing the ionic interaction between PEDOT and PSS through hydrogen bonding. This, in turn, facilitates better phase separation between the two components, leading to improved electrical conductivity [56,57]. Additionally, the presence of PEG promotes the aggregation of PEDOT particles on the surface of NWF after NIPS coating treatment. This aggregation reduces inter-chain or inter-domain charge bounding, resulting in enhanced charge transfer within the 3D connected PEDOT particles [57]. To form a chemically and mechanically stable hybrid thin film, PEG is functionalized with chemical linkages to both the conductive PEDOT:PSS film and the NWF substrate [57,69,70]. Similarly, when considering the PEI:rGO deposition process, it is reasonable to expect that PEI:rGO laminates can infiltrate the porous topology of the PEDOT:PSS/PEG structure. During the electrochemical process, the PEI:rGO could be ionically interacted through crosslinking of amine groups with the sulfonyl and amino groups of PSS and PEG molecules, respectively, further reinforcing the structure [26,30,46,57,71]. A schematic representation of this plausible mechanism is provided in Fig. SI-17, ESI 1.

The Raman spectra of P:P:P and PEI:rGO/P:P:P membranes were also
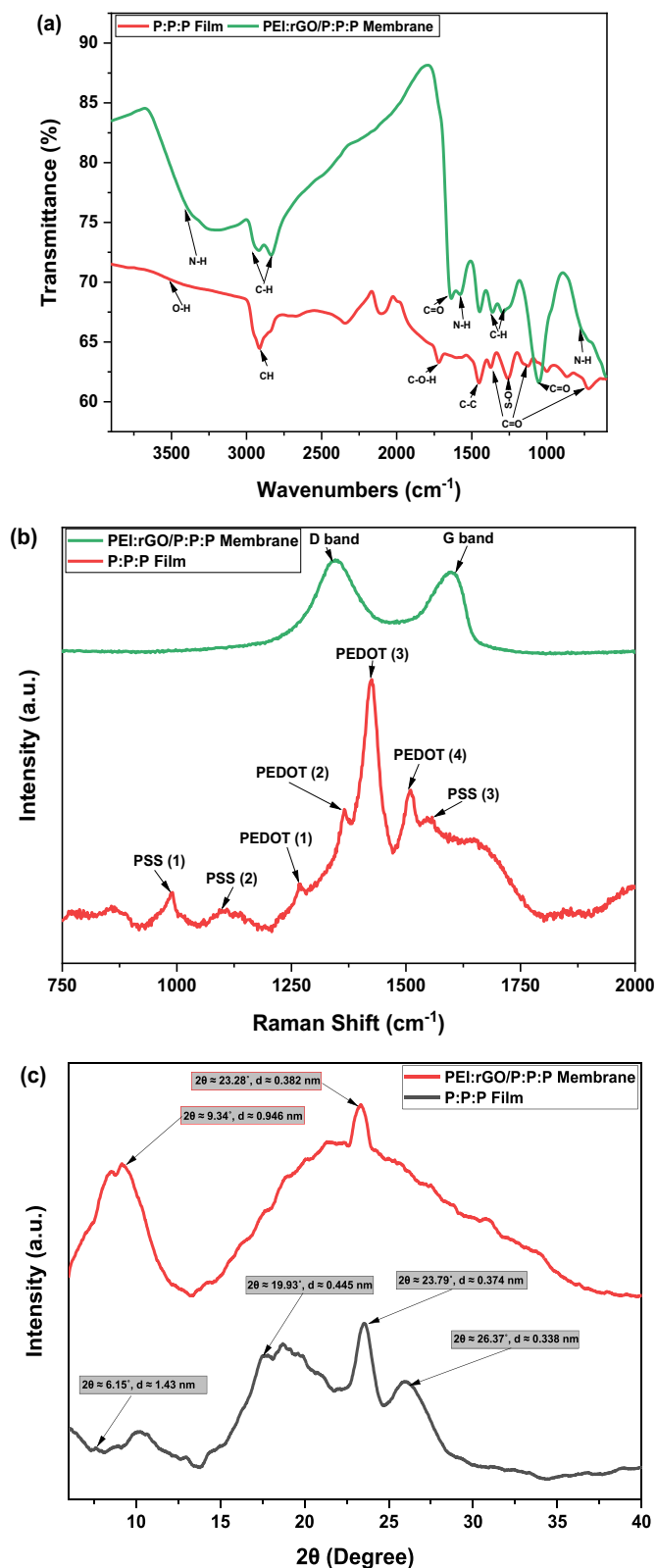
Fig. 4. (a) FTIR spectra, (b) Raman spectra, and (c) XRD patterns of the as-prepared P:P:P conductive film and PEI:rGO/P:P:P composite membrane.

studied Fig. 4.b. For the P:P:P film, vibrational modes of PEDOT were identified at 1518 cm^{-1}, 1482 cm^{-1}, 1345 cm^{-1}, and 1280 cm^{-1}, corresponding to different inter-ring bonds stretching vibrations. Vibrational modes of PSS were located at 1120 cm^{-1} and 992 cm^{-1}, attributed

to (O—S stretching) and (C—S—C stretching), respectively. The Raman shift of (C—C asymmetric stretching) at 1583 cm^{-1} indicated a reduction in the intensity of certain fingerprints, indicating partial removal of PSS from the outer shell of the PEDOT molecule, which might be interacted with PEG molecule and PEI:rGO sheets [29,31,32,72,73]. However, no clear observation of PEG was noticed in the Raman spectrum of PEDOT:PSS/PEG (P:P:P) film. On the other hand, the addition of PEI to the rGO for PEI:rGO/P:P:P membrane led to changes in the Raman spectra, showing the partial removal of oxygen-containing functional groups and the transition of sp^3 carbon into sp^2 carbon in the PEI:rGO sample [26,58,67,74]. The electrical conductivity obtained from this modified rGO, with shorter and broader *D* and *G* bands positioned at 1344.9 cm^{-1} and 1598.6 cm^{-1} (I$_D$/I$_G$ ~ 1.15), could be sufficiently high for electro-oxidation processes [24].

XRD diffraction patterns for prepared P:P:P and PEI:rGO/P:P:P membranes were investigated (Fig. 4.c). In the PEDOT:PSS/PEG film, four peaks were observed at 2θ values of approximately 6.15°, 19.93°, 23.79°, and 26.37°, corresponding to lattice d-spacings associated with π–π lamella stacking and inter-chain ring stacking between PEDOT:PSS [31,75–77]. The addition of PEG showed negligible changes in the d-spacing, indicating that the amino group of PEG had no significant effect on the crystal structure of PEDOT:PSS [32]. After deposition of modified rGO, the PEI:rGO/P:P:P membrane exhibited two distinct peaks at 2θ values of 9.34° and 23.28° with corresponding d-spacings of 9.46 Å and 3.82 Å, respectively. The first peak indicated the presence of un-exfoliated GO, while the sharp peak at 23.28° suggested partial removal of functional groups due to the incorporation of PEI [26,67,78]. Although the d-spacing effects on electrical conductivity might be obscured by the high defect rates in PEI:rGO [24], a uniform coating of reconstructed PEI:rGO flakes with smaller interlayer space is expected to enhance salt-rejection efficiency, while the presence of GO could improve membrane hydrophilicity and water permeability.

3.4. Membrane conductivity

The primary goal of this study is to develop novel PEI:rGO/P:P:P composite membranes with an improved electrical conductivity. This can effectively aim to enhance anti-fouling and desalination performances of modelled seawater (*i.e.*, water with different cations and anions) in an FO process through separating charged ions by applying an electrical field, considering advantages of ionisable functional groups attached to the PEI:rGO active layers [21,79]. Here, the obtained electrical resistance and conductivity values of the prepared membranes are shown in Table 2. The corresponding electrochemical impedance spectra (EIS) of the membranes using Nyquist curves, which revealed single relaxation behavior with indicative of Debye behavior, are illustrated in Fig. SI-18, ESI 1. The results indicated that the NWF sample, without any PEDOT:PSS/PEG coating, had the lowest electrical conductivity. In contrast, the P:P:P samples with PEDOT:PSS/PEG depositions demonstrated significantly enhanced electrical conductivity, surpassing the PEI:rGO-based membranes by 5 to 6 times [28,32,34]. Moreover, herein, the intensity of membrane coating (*i.e.*, P:P:P and PEI:rGO) plays an important role for enhancement of electrical conductivity [24]. The improvement in electrical conductivity for the P:P:P samples can be attributed to the creation of more charge carriers in the polymer matrix at the percolation threshold [34]. These carriers find electrical

Table 2
Electrical resistance and conductivity measurements of membrane samples.

Sample	Resistance (R, Ohms)	Conductivity (k, S/m)
NWF	48,880 ± 401	0.07 ± 0.006
SS-P:P:P	132.9 ± 7.55	26.5 ± 1.785
DS-P:P:P	99.24 ± 5.92	35.3 ± 3.112
SS-PEI:rGO	676.8 ± 35.1	5.2 ± 0.315
DS-PEI:rGO	636.5 ± 32.8	5.5 ± 0.321

pathways to facilitate efficient charge transport. On the other hand, the conductivity mechanism in the PEI:rGO films is influenced by factors such as structural defects, functionality, and layer disorder of the graphene layers [26,40]. The reduction treatment duration during the preparation of PEI:rGO films also affects their electrical conductivity. While higher reaction temperatures may create highly conductive networks, the interlayer spacing of modified rGO laminates can be decreased, making the membranes impermeable to water molecules [24]. Notably, the use of a small PEI:GO ratio (PEI:rGO-0.01) significantly improved the electrical conductivity of the resulting rGO. However, increasing the PEI content would dramatically reduce the electrical conductivities of the rGO due to nonconductive PEI being chemically attached to the rGO surface [26]. Nonetheless, the tunable electrical conductivity of PEI:rGO membranes makes them promising for water treatment applications through electro-oxidation processes.
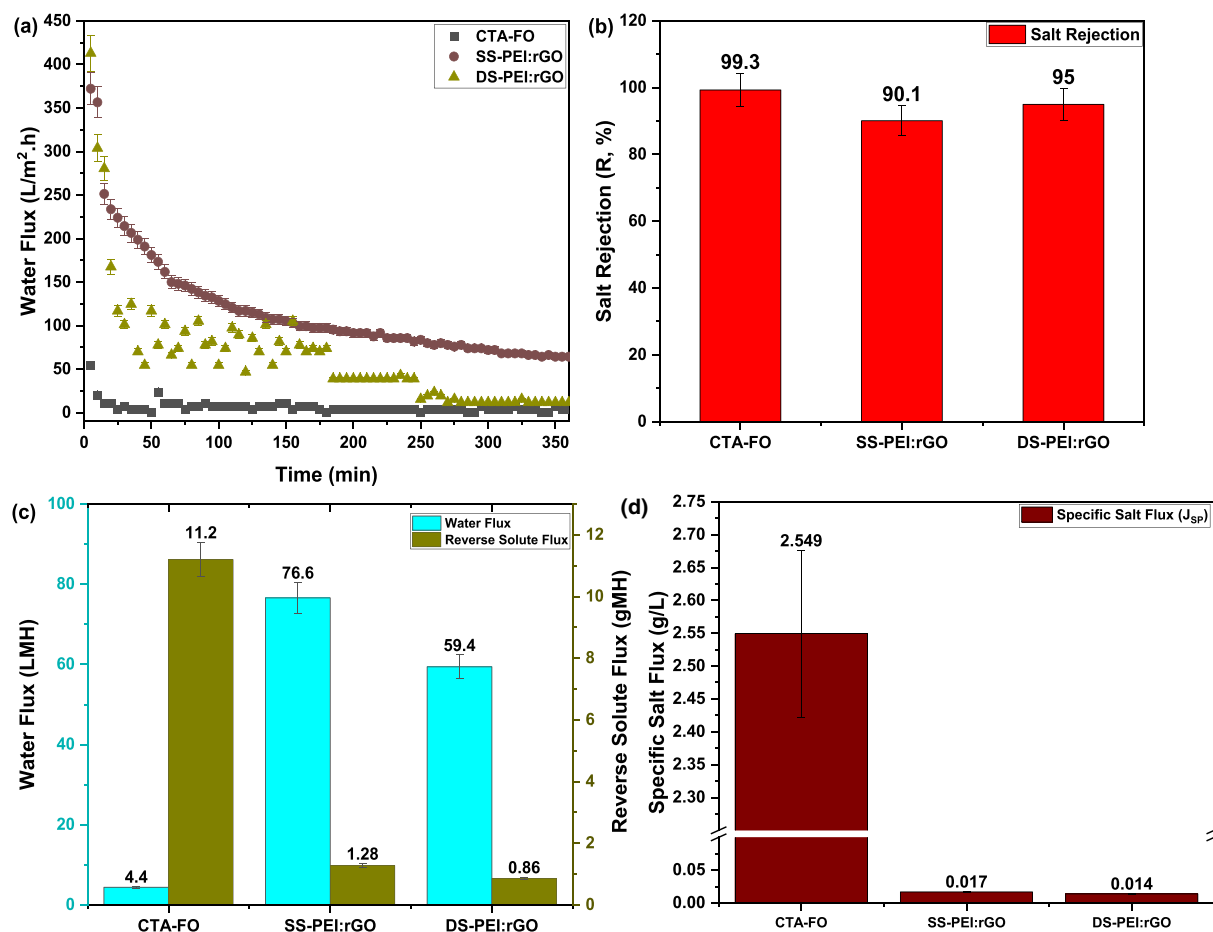
3.5. FO membranes performance

Upon optimizing the deposition time for PEI:rGO-based membrane fabrication (see section SI-4, ESI 1), comparison tests for two types of membranes, SS-PEI:rGO and DS-PEI:rGO, with the commercially available CTA-FO membrane were conducted in FO processes, specifically FO desalination and ICP evaluation tests. Our findings, encompassing water permeation rates, salt retention, reverse solute flux, and selectivity, are presented in Fig. 5. To assess the salt rejection capabilities of the membranes in FO, a lab-scale FO system was operated using a 0.1 M NaCl solution as the feed solution and 0.5 M dextrose as the draw solution. Fig. 5 (a) shows the water flux across each membrane, revealing that the SS-PEI:rGO membrane exhibits the highest water flux (mean value: 117 LMH), followed by the DS-PEI:rGO membrane (63.9 LMH), and lastly, the commercial CTA-FO membrane (5.91 LMH). In Fig. 5.b, the SS-PEI membrane (90.1 %) exhibited a slightly lower salt rejection compared to the DS-PEI:rGO membrane (95 %) and CTA-FO membrane (99.3 %). This observation implies that the SS-PEI:rGO membrane allowed more ions to pass through in comparison to the DS-PEI:rGO membrane. The reason behind this could be attributed to the increased pore size and pore volumes in the SS-PEI:GO membrane [27,53]. The limited diffusion of PEI:rGO laminates through the SS-P:P:P substrate may have failed to effectively block microspores within the structure of the membrane, in contrast to the DS-P:P:P support layer.

In Fig. 5 (c), the average water flux (J_w) and reverse solute leakage (J_s) through the membranes were measured in FO experiments using 0.6 M NaCl solution as the draw solution and DI water as the feed solution. The study investigated three types of membranes: SS-PEI:rGO, DS-PEI:rGO, and CTA-FO. The results showed that in the FO mode, the mean water flux values were 76.6, 59.4, and 4.4 LMH for SS-PEI:rGO, DS-PEI:rGO, and CTA-FO membranes, respectively. Among these membranes, the DS-PEI:rGO membrane had the lowest reverse solute flux at 0.86 gMH, followed by the PEI:rGO membrane (1.28 gMH) and the commercial CTA-FO membrane (11.2 gMH). The reverse solute diffusion observed in the FO process can negatively impact the efficiency of the process by reducing the osmotic pressure, contaminating the feed solution, and triggering a loss of the draw solute [46,54,80]. The introduction of a highly porous and hydrophilic support layer, however, can help minimise the osmotic pressure drop [53]. In our study, it was found that the high-water flux hindrance caused by the support layer led to an osmotic pressure gradient between the bottom of the support layer and the active layer interface. The DS-PEI:rGO membrane addressed this hindrance through double-coating and Donnan effect mechanisms [13,46,61,81]. However, the thicker dense layer resulting from the double-sided deposition of DS-PEI:rGO might be a reason for its lower water flux compared to the SS-PEI:rGO membrane. Furthermore, salts rejected by the SS-PEI:rGO layer could accumulate in the salt-permeable P:P:P coating layer due to the repulsive force of sulfonic groups towards the anions (Cl$^-$), leading to slight concentration polarisation within the P:P:P coating layer [46]. The specific salt flux (J_{SP}) was used as an

Fig. 5. (a) Water permeation rates and (b) salt rejection efficiency of as-prepared PEI:rGO membranes compared to the commercial CTA-FO membrane, being evaluated in FO mode using 0.1 M NaCl solution and 0.5 M dextrose as feed and draw solutions, respectively. (c) Water flux and reverse solute permeation, and (d) specific salt flux of CTA-FO and PEI:rGO-based membranes, being assessed for level of salt rejection of the active layer across membranes with DI water and 0.6 M NaCl solution were used as feed and draw solutions at room temperature, respectively.

important parameter to assess FO membrane efficiency by representing the level of salt rejection across the active layer of the membrane [47], and it was found that DS-PEI:rGO, SS-PEI:rGO, and CTA-FO membranes achieved rejection ratios of 0.014, 0.017, and 2.549 g/L, respectively. This was owing to the significant decrease of the RSF values than the water flux rates of DS-PEI:rGO membrane compared to the SS-PEI:rGO and CTA-FO membranes, respectively. This could partially compromise the effects of ICP across the PEI:rGO-based membranes, which is in a good agreement with the reported literatures [47,82,83].

To confirm the effect of reducing RSF across the membranes, in the FO-ICP evaluation test, the concentration of ion permeation through different membranes over time was examined, and the results are depicted in Fig. SI-20, ESI 1. As anticipated, the NWF membrane exhibited the highest permeability to sodium and chloride ions, followed by SS-P:P:P, DS-P:P:P, CTA-FO, SS-PEI:rGO, and DS-PEI:rGO membranes. Notably, the DS-PEI:rGO membrane showed a reduction of approximately 31.2 % in the ion permeation rate compared to the SS-PEI:rGO membrane. These findings highlight the varying degrees of ion permeability among the tested membranes, with NWF being the most permeable and DS-PEI:rGO displaying the lowest permeation rate, indicating its potential for specific applications requiring controlled ion transport. This confirmed that the DS-PEI:rGO membrane exhibited higher ion rejection capability for desalination compared to the SS-PEI:rGO membrane. However, the DS-PEI:rGO membrane also showed a lower water permeation rate due to the additional P:P:P and PEI:rGO layers on the membrane, but these slightly retarded ion permeation as compared to SS-PEI:rGO. The obtained findings are in a good agreement

with the intrinsic transport properties demonstrated in (Section SI-2, ESI 1). Here, results demonstrated that the DS-PEI:rGO membrane offered the best overall performance in terms of ion rejection while maintaining reasonably good water permeation compared to the SS-PEI:rGO membrane.

3.6. Membrane anti-fouling properties

Enhancing the anti-fouling propensity of membranes is crucial for ensuring the long-term stability of large-scale desalination plants [84]. Fouling propensity significantly affects the membrane separation performance and operational lifespan, as it involves the accumulation of foulant molecules on the membrane selective layer. This fouling can occur through various mechanisms, such as electrostatic interactions, hydrophobic effects, hydrogen bonding, and London–van der Waals attractions. These mechanisms can block the pore entrances, impeding water permeation through the membrane structure [40,85,86]. In this study, the anti-fouling ability of two types of membranes, SS- and DS-PEI:rGO, was investigated and compared to the commercial CTA-FO membrane. SA was selected as a model foulant and bridging agents like calcium, sodium, chloride, and sulfate ions were used during experiments conducted under FO mode to evaluate the interaction of foulants with the membrane active surface layers. Fig. 6.a illustrates the evolving FO normalized water fluxes for the membranes when exposed to a high concentration of SA (1000 ppm). Beside the commercial CTA-FO membrane, both PEI:rGO membranes (under DC and no DC voltage) exhibited various decline levels in water flux during the initial 80 min,
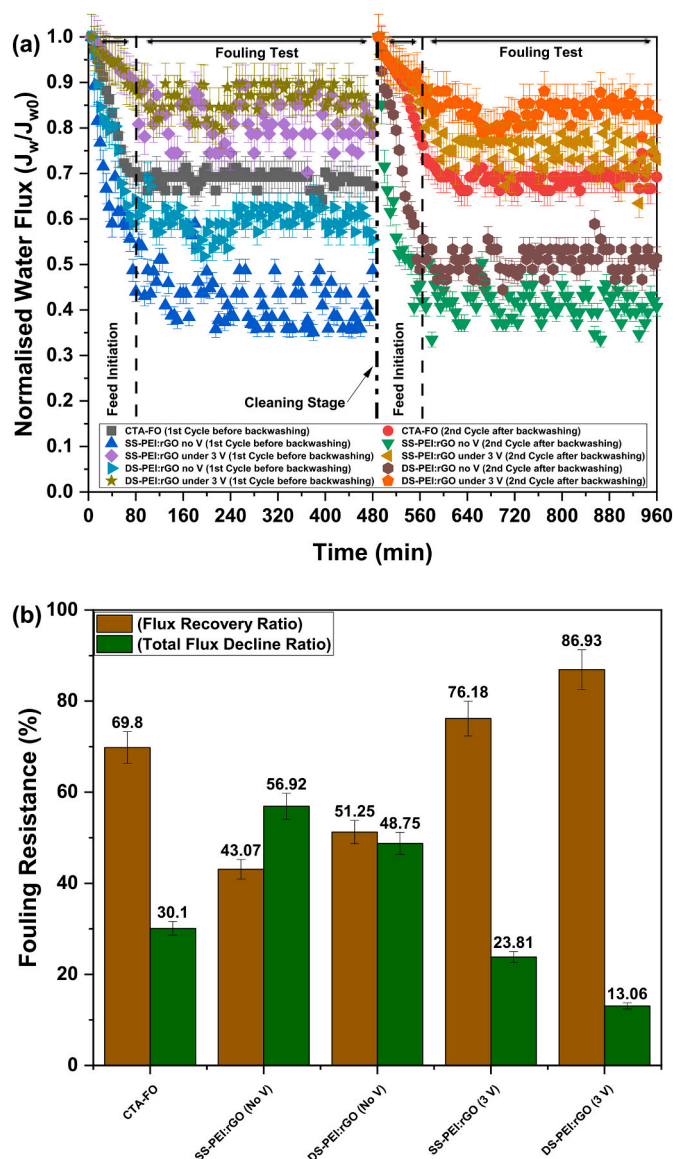
Fig. 6. (a) Normalized water flux profiles during fouling experiments in FO process, and **(b)** anti-fouling properties (*recovered flux and water flux decline ratios*) of as-prepared SS-PEI:rGO and DS-PEI:rGO membranes (*under both no voltage and optimum voltage of 3 V*), compared to that of commercial CTA-FO membrane.

which can be attributed to a reduction in draw solution concentration before adding foulants [85]. Upon the addition of SA foulants, both PEI:rGO membranes (under no DC potential) showed a higher decline in water flux, comparable to the SS- and DS-PEI:rGO (under 3.0 V) and CTA-FO membranes, indicating adsorption of SA macromolecules on the surfaces leading to membrane fouling. It is noteworthy that CTA-FO membrane exhibited a stable flux, compared to PEI:rGO-based membranes, despite it is being a non-electrical conducting membrane. This is primarily due to its uniform pore structure, consistent engineered performance, optimized surface properties, and precise manufacturing processes, which can maintain reliable and consistent filtration performance over a certain time [87,88]. These findings are supported by our SEM and NPFlex morphology and structure observations, as shown in Fig. SI-24, ESI 1 and Fig. SI-26, ESI 1, respectively. After backwashing process, the water flux decline rates for PEI:rGO membranes (under no DC potential) slightly increased during the second cycle test, confirming severe membrane fouling. Notably, the PEI:rGO membranes (with zero DC potential) experienced more severe fouling than the commercial

CTA-FO membrane under the same conditions Fig. 6.a. This more sever fouling is due to SA macromolecules adsorbing immediately onto the membrane surface and clogging water pass channels [89]. In the course of this investigation, when no voltage was administered during the fouling protocol process, the water flux of PEI:rGO-based membranes primarily relied on the intricate characteristics of its pore structure Fig. 6.a. However, by applying an optimized electric potential of 3.0 V to both PEI:rGO membranes, water flux trends were significantly increased, this indicated a drastic decline in membrane fouling during the two-cycle fouling protocol tests. This remarkable anti-fouling property observed in the PEI:rGO-based membranes can be attributed to the electro-oxidation process induced on the surface by the DC potential [28,40]. Slight bubbling of oxygen on the surface of membrane due to an electro-oxidation process induced higher feed re-circulation and drag forces, preventing foulant diffusion into the open pores and thus increasing water flux [90]. DS- and SS-PEI:rGO membranes (with no voltage) lost flux more rapidly and were more severely fouled compared to the prepared PEI:rGO membranes evaluated under 3.0 V and the commercial FO-CTA membrane Fig. 6.b. The DS-PEI:rGO (3.0 V) membrane exhibited the best performance with the least total flux decline ratio value and the highest water recovery, indicating superior anti-fouling behavior in Fig. 6.b. The study suggests that factors such as surface charge, roughness, and hydrophilicity influence the anti-fouling behavior of water treatment-based membranes [27,85]. The presence of negatively charged GO sheets could function as a repulsive agent, facilitating the repulsion of negatively charged SA foulants *via* electrostatic repulsion, applicable only in the hybrid electro-oxidation/membrane process by applying DC potential [40]. Surface elemental analysis confirmed reduced deposition of Na^+, Cl^-, Ca^{2+}, and S^{2-} ions during the electro-oxidation process for the PEI:rGO membranes compared to those assessed under no electric potential (Fig. SI-21, ESI 1). Electrical conductivity measurements and surface roughness data also supported the findings, as presented in Table SI-5 and Fig. SI-23 and SI-26, ESI 1. Another critical parameter, but less significant than the surface charge, could be the surface roughness of membranes. Generally, less rough surfaces with an extended surface area potentially provide less space for adhesion of foulants, making them less susceptible to fouling [27,85]. Conclusively, the PEI:rGO-based membranes, particularly the DS-PEI:rGO (3.0 V) membrane, demonstrated enhanced anti-fouling properties, primarily attributed to the application of DC potential, surface charge, and surface roughness. These findings have significant implications for improving the stability and performance of desalination plants. For further details and models, refer to Section (SI-5, ESI 1).

3.7. Stability performance assessment

Our study highlights the significance of using PEI:rGO laminates, in combination with a P:P:P interfacial layer, in enhancing the structural integrity and durability of membranes, with promising characteristics for FO desalination applications. It should be noted that CTA-FO membranes generally exhibited superior chemical and mechanical stability under different pH levels and mechanical stresses without significant degradation [87,91–93]. This has been consistent with our stability performance assessment observations for the commercial CTA-FO membrane during chemical and mechanical testing (*supported by Table SI-6, ESI 1*), compared to that of P:P:P and PEI:rGO membranes. Therefore, in this work, a thorough assessment of the structural integrity and durability was only conducted and included for SS-P:P:P, DS-P:P:P, SS-PEI:rGO, and DS-PEI:rGO membranes. To compare their performance, these membranes were immersed in a 0.6 M NaCl solution, as depicted in Fig. 7.a and Fig. SI-29, ESI 1. The results were compelling and showed distinct behaviours for each type of membrane. The SS-P:P:P and DS-P:P:P membranes experienced disintegration starting from day 100, while the SS-PEI:rGO membrane began to decompose gradually from day 80. Surprisingly, the DS-PEI:rGO membrane maintained its

(a)	**(Exposure Time in 0.6 M NaCl)**								
Membrane	*Day 0*	*Day 10*	*Day 20*	*Day 30*	*Day 40*	*Day 60*	*Day 80*	*Day 100*	*Day 120*
SS-P:P:P	5	5	5	5	5	5	5	4	4
DS-P:P:P	5	5	5	5	5	5	5	4	3
SS-PEI:rGO	5	5	5	5	5	5	4	3	2
DS-PEI:rGO	5	5	5	5	5	5	5	5	4

Excellent (Score: 5)   Good (Score: 4)   Fair (Score: 3-2)   Poor (Score: 1-0)

(b)		**(Exposure Time in NaClO)**											
Concentration		*0 h*				*8 h*				*24 h*			
30,000 ppm		3	4	5	5	1	4	5	5	0	1	2	3
10,000 ppm		4	5	5	5	3	4	5	5	0	2	3	4
1,000 ppm		5	5	5	5	4	4	5	5	0	3	4	4

Excellent (Score: 5)
Good (Score: 4)
Fair (Score: 3-2)
Poor (Score: 1-0)

SS-P:P:P	DS-P:P:P	SS-PEI:rGO	DS-PEI:rGO	SS-P:P:P	DS-P:P:P	SS-PEI:rGO	DS-PEI:rGO	SS-P:P:P	DS-P:P:P	SS-PEI:rGO	DS-PEI:rGO

(Membrane Sample)

Fig. 7. Dimensional stability and durability of conductive substrates and rGO-based membranes (*following an industrial score rating*), being exposed to **(a)** 0.6 M NaCl ionic solution, and **(b)** NaClO ionic solution with different concentrations.

initial state for an extended period of 120 days without any damage. The exceptional durability of the DS-PEI:rGO membrane can be attributed to the role of the PEI cross-linker. By creating multiple bonds with neighbouring GO nanosheets, the PEI cross-linker significantly enhanced the structural integrity of the membrane, preventing the separation of GO nanosheets [51,60,61]. Additionally, the PEI cross-linker formed strong ionic bonds with the PEDOT:PSS/PEG molecules, further contributing to the membrane's ability to retain its original structure. These findings demonstrate a clear advantage of using PEI:rGO laminates to double coat both sides of the P:P:P membranes. This approach not only improved the structural integrity and durability but also ensured that the membrane maintained its stability during the ionic testing with NaCl. On the other hand, the SS-PEI:rGO membrane had stability issues due to some PEDOT:PSS/PEG molecules forming weaker bonds with the PEI:rGO sheets. Consequently, this membrane could not hold the PEI:rGO laminates firmly enough to preserve its initial structure during the NaCl ionic testing.

The chlorine tolerance of prepared P:P:P and PEI:rGO-based membranes was assessed by subjecting them to aqueous solutions of sodium hypochlorite (NaOCl) with concentrations of 1000, 10,000, and 30,000 ppm. It is worth noting that in industrial processes, only a few ppm of chlorine are typically used for the membrane cleaning process [54]. Fig. 7.b and Fig. SI-30, ESI 1 show the results of the chlorine tolerance test for DS-PEI:rGO, SS-PEI:rGO, DS-P:P:P, and SS-P:P:P membranes. The DS-PEI:rGO membrane exhibited the highest chlorine resistance when exposed to high ppm concentrations of chlorine for 8 h at room temperature, followed by the SS-PEI:rGO, DS-P:P:P, and SS-P:P:P membranes in descending order of chlorine resistance. However, when the exposure time to chlorine was extended to 24 h, the PEI:rGO-based membranes started losing their structural integrity, while the P:P:P-based membranes were completely damaged. This deterioration is attributed to the decomposition of ionic bonding between PEDOT:PSS/PEG molecules and PEI:rGO laminates due to the strong chlorine effect [94,95]. Additionally, the hydrogen bonding between PEDOT:PSS/PEG molecules and NWF is completely diminished over the same duration,

possibly due to the limiting effect of Na^+ [96]. These findings are consistent with the observations made during dipping tests in a 0.6 M NaCl solution.

To assess the long-term dimensional stability of the prepared membranes, P:P:P substrates and PEI:rGO-based membranes were subjected to sonication in DI water for varying durations. In Fig. 8.a and Fig. SI-31, ESI 1, it is evident that all membranes maintained good dimensional stability during 60 min of sonication. However, the SS-PEI:rGO membrane gradually started to collapse after this time, DS-P:P:P, SS-P:P:P, and DS-PEI:rGO membranes remained unchanged and exhibited excellent structural integrity for over 100 min. While the outstanding mechanical stability of the P:P:P substrates remains poorly understood, the DS-PEI:rGO membrane securely anchors PEI:rGO sheets with the PEDOT:PSS/PEG molecules, even under conditions of static and shearing stress [97].

The durability of both prepared SS-PEI:rGO and DS-PEI:rGO membranes was investigated during the fouling process, and the results are illustrated in Fig. SI-32, ESI 1. Digital images of the SS-PEI:rGO and DS-PEI:rGO membranes after >16 h of operation, showed no signs of defects or fractures on the membrane surface. However, when comparing the corresponding FE-SEM images of the SS-PEI:rGO and DS-PEI:rGO membranes, a notable difference emerged. The SS-PEI:rGO membrane, which had been subjected to prolonged use under continuous pulsating flow (shear stress of the fluid) from the gear pump, displayed abrasion on both the P:P:P and PEI:rGO layers. Consequently, the efficiency of this membrane decreased with extended operation time, leading to increased permeation of salt ions through its surface. Furthermore, the integrity of the PEI:rGO layer, along with the P:P:P interfacial layer, was compromised, making it susceptible to detachment from the NWF sublayer. In contrast, the DS-PEI:rGO membrane exhibited remarkable stability during the fouling test, remaining unchanged even after operating for several hours. This outcome confirmed that the double-coating protocol had significantly improved the structural stability of the membrane. In summary, the results indicated that the DS-PEI:rGO membrane outperformed the SS-PEI:rGO membrane in terms of

(a)	(Structural durability in ultrasonication)		
Membrane	*0 min*	*≥ 60 min*	*≤ 100 min*
SS-P:P:P	5	5	5
DS-P:P:P	5	5	5
SS-PEI:rGO	5	4	3
DS-PEI:rGO	5	5	4

Stable (Score: 5)   Disassembled (Score: 4)
Deformed (Score: 3-2)   Critically damaged (Score: 1-0)
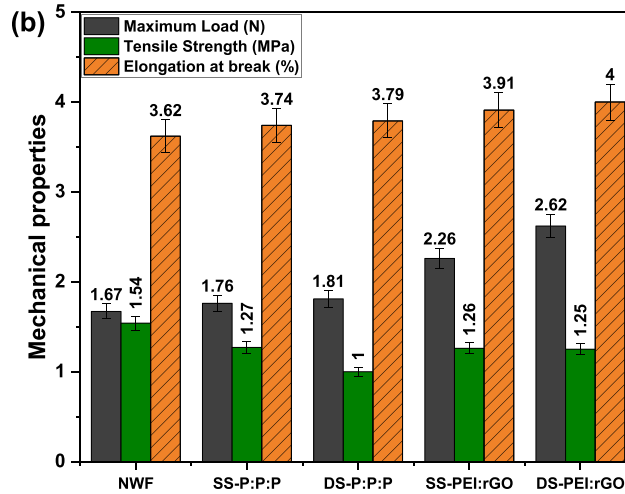
Fig. 8. Evaluation of mechanical integrity and durability of membranes, during **(a)** ultrasonication testing (*following an industrial score rating process*), and **(b)** tensile strength testing.

durability and structural stability, making it a more reliable option for prolonged operation under the fouling process. In addition, the mechanical stability of our prepared PEI:rGO membranes during fouling tests relied on the strong chemical binding between PEI:rGO laminates and P:P:P molecules. Moreover, the application of DC voltage, which leads to oxygen bubbling on the membrane surface, did not have significant effect on the integrity of the membrane.

In an ideal FO system, the membrane should primarily experience shear stress resulting from the friction between the membrane surface and cross-flow fluids [27,53,98]. Several factors could impact the membrane usage, including the properties of the raw materials, methodologies and parameters of fabrication, incorporation of doping additives, and considerations of structural characteristics such as porosity and tortuosity [99]. Consequently, it is of a great importance to further investigate the dimensional stability of the membranes. To evaluate the mechanical properties of the prepared membranes in comparison to NWF, various mechanical integrity tests were conducted, and the results are presented in Fig. 8.b and Fig. SI-33, ESI 1. In most cases, NWF films are predominantly produced *via* the electrospinning technique, which inherently results in enhancing internal porosity [100]. Therefore, the NWF layer had a higher mechanical strength, but a lower elongation rate compared to the other modified membranes. Among the prepared P:P:P membranes, the DS-P:P:P membrane demonstrated the lowest tensile strength, but a slightly higher elongation rate compared to the SS-P:P:P and NWF membranes. This behavior is attributed to the influence of acid dopants on the intermolecular reconfiguration of the DS-P:P:P film during the dual-coating procedure, consequently leading to a reduction in membrane strength. Notably, the DS-PEI:rGO membrane exhibited the highest elongation rate among all the tested membranes. This can be

attributed to several factors. Firstly, the method of preparation involved the double-coating of P:P:P mixture with chemically stable PEI:rGO laminates, which allowed for their effective interconnection on the NWF film. Another possible reason for the enhanced mechanical strength of the DS-PEI:rGO membrane could be the slight percolation of acid from the P:P:P membranes during the electrochemical process [56]. These characteristics contribute to its overall mechanical robustness and superior performance.

Table 3 summarises the performance of our prepared membranes, SS-PEI:rGO and DS-PEI:rGO in comparison with other conductive membranes used in forward osmosis studies for water treatment. Our membranes demonstrated superior water flux, NaCl ion selectivity, and dimensional stability compared to those reported in other research works [20,40]. It is worth noting that the anti-fouling performance under a DC electric potential of our membranes was not as high as that reported in the literature [40]. This difference could be attributed to the distinct behavior of hybrid electro-oxidation/membrane materials, operating through direct and indirect oxidation mechanisms which was utilized in the work by Rastgar et al. [40]. Overall, our findings highlight the exceptional characteristics of the SS-PEI:rGO and DS-PEI:rGO membranes, which outperformed other conductive membranes in various aspects, making them promising candidates for forward osmosis applications. However, further research is needed to fully understand the mechanisms behind the varying anti-fouling performance and optimize the electrochemical properties of the membranes (refer to Section SI-5, ESI 1). Furthermore, it is worth noting while the mechanical integrity of rGO membranes fabricated in this work is comparable to the commercial CTA-FO membrane, their chemical stability may be compromised by their significantly higher antifouling and desalination

Table 3

Comparison of electrochemical properties, water permeation, salt selectivity, and stability of conductive rGO-based membranes, being assessed in a laboratory-scale FO system.

Membrane	Fabrication method	Water treatment process	R (Ω)/K (S/m)	Water flux (LMH)	Selectivity (g/L)	Anti-fouling FRR/R_t (%) under DC voltage	Stability	Ref.
SS-PEI:rGO	EPD	FO	498.1/8.1	117.2	0.014 (NaCl)	76.18/23.81 **(3.0 V)**	Good Mech./Chem.	This Work
DS-PEI:rGO	EPD	FO	622.1/6.4	79.8	0.015 (NaCl)	86.93/13.06 **(3.0 V)**	High Mech/good Chem.	This Work
rGO/CNT	EPD	FO	–	22.6	0.07 (NaCl)	–	Excellent Chem.	[20]
rGO/PSF	Dead-End Filtration	FO	4984/1.8	10.5	1.48 (NaCl)	99/1.3 **(2.0 V)**	Low Mech.	[40]

performances under electrical potential.

4. Conclusion

In this research, a newly developed method was employed to create PEI:rGO/P:P:P-based membranes through electrophoretic deposition. The membranes were subjected to various tests, including FO desalination, ICP evaluation, and fouling experiments using monovalent salt ions and organic SA to assess their antifouling properties. The physico-chemical and morphological analyses confirmed the successful and tight combination of PEI:rGO laminates with the P:P:P substrates by applying an optimized DC potential of 10 V in a one-step electro-chemical approach. Upon assembling PEI:rGO laminates on the P:P:P membranes, the electrical conductivity of the resulting SS- and DS-PEI:rGO membranes decreased due to the chemical reduction process of graphene oxide. However, the PEI crosslinked rGO maintained sufficient hydrophilicity to facilitate water permeability across the membranes, as evidenced by higher water contact angles compared to P:P:P substrates. In FO experiments, the SS- and DS-PEI:rGO membranes exhibited superior desalination performance, with improved water permeation and ion selectivity compared to the commercial CTA-FO membrane. By applying an optimal electrical potential of 3.0 V, the fouling behavior of the fabricated PEI:rGO-based membranes significantly improved, resulting in stabilized water flux without any decline even after multiple testing cycles. The improved performance was attributed to direct and indirect oxidation reaction mechanisms. Moreover, the PEI:rGO-based membranes demonstrated structural integrity and long-term durability when subjected to mechanically harsh and high ionic strength environments. The bonding investigation between PEI:rGO sheets and PEG functionalized PEDOT:PSS suggested that the membranes possess structural robustness due to a membrane-wide network of ionic bonds arising from interactions between the PEI:rGO sheets and the aligned PEDOT:PSS/PEG chains. This study offers a promising direction for developing high-performance FO membranes by utilizing functionalized rGO, with significant potential for water purification applications. Nonetheless, further optimisation and research are needed, particularly in enhancing the conductivity of the PEI:rGO/P:P:P membranes to mitigate potential drop issues during the FO fouling process and running process for a long-term. Furthermore, future research endeavours will extend beyond the assessment of the resultant membranes to examine their anti-fouling performance under the electrical potential concerning also inorganic foulants within the context of the FO desalination process.

Supplementary data to this article can be found online at https://doi.org/10.1016/j.jwpe.2024.104809.

CRediT authorship contribution statement

Mohamed Edokali: Writing – review & editing, Writing – original draft, Methodology, Investigation, Formal analysis, Data curation, Conceptualization. **Mozhdeh Mehrabi:** Writing – review & editing, Methodology, Data curation. **Oscar Cespedes:** Writing – review & editing, Methodology, Data curation. **Chao Sun:** Writing – review & editing, Methodology. **Sean M. Collins:** Writing – review & editing, Methodology. **David Harbottle:** Writing – review & editing, Supervision. **Robert Menzel:** Writing – review & editing, Supervision, Methodology, Investigation, Formal analysis, Conceptualization. **Ali Hassanpour:** Writing – review & editing, Supervision, Methodology, Investigation, Formal analysis, Conceptualization.

Declaration of competing interest

The authors want to emphasize that no competing commercial interests could potentially influence or bias the results, findings, or conclusions presented in this work. We also affirm that our primary focus is solely on the scientific integrity and objective reporting of our research. Hence, there are no conflicts of interest related to any financial, proprietary, or personal affiliations that could compromise the impartiality and credibility of the study.

Data availability

Data will be made available on request.

Acknowledgment

References

[1] R.V. Linares, et al., Forward osmosis niches in seawater desalination and wastewater reuse, Water Res. 66 (2014) 122–139.

[2] C. Klaysom, et al., Forward and pressure retarded osmosis: potential solutions for global challenges in energy and water supply, Chem. Soc. Rev. 42 (16) (2013) 6959–6989.

[3] W. Xu, Q. Chen, Q. Ge, Recent advances in forward osmosis (FO) membrane: chemical modifications on membranes for FO processes, Desalination 419 (2017) 101–116.

[4] S. Zhao, et al., Recent developments in forward osmosis: opportunities and challenges, J. Membr. Sci. 396 (2012) 1–21.

[5] M. Xie, et al., Role of pressure in organic fouling in forward osmosis and reverse osmosis, J. Membr. Sci. 493 (2015) 748–754.

[6] W. Wu, et al., Recent development of graphene oxide based forward osmosis membrane for water treatment: a critical review, Desalination 491 (2020) 114452.

[7] J. Wang, X. Liu, Forward osmosis technology for water treatment: Recent advances and future perspectives, J. Cleaner Prod. 280 (2021) 124354.

[8] N. Akther, et al., Recent advancements in forward osmosis desalination: a review, Chem. Eng. J. 281 (2015) 502–522.

[9] I. Ndiaye, S. Vaudreuil, T. Bounahmidi, Forward Osmosis Process: State-of-the-art of Membranes, in: Separation & Purification Reviews, 2019, pp. 1–21.

[10] N. Abounahia, et al., Desalination by the forward osmosis: advancement and challenges, Sci. Total Environ. 886 (2023) 163901.

[11] X. Chen, et al., Enhanced performance of cellulose triacetate membranes using binary mixed additives for forward osmosis desalination, Desalination 405 (2017) 68–75.

[12] T.P.N. Nguyen, et al., Preparation of cellulose triacetate/cellulose acetate (CTA/CA)-based membranes for forward osmosis, J. Membr. Sci. 433 (2013) 49–59.

[13] E. Yang, et al., Enhanced desalination performance of forward osmosis membranes based on reduced graphene oxide laminates coated with hydrophilic polydopamine, Carbon 117 (2017) 293–300.

[14] M.M. Pendergast, E.M. Hoek, A review of water treatment membrane nanotechnologies, Energy Environ. Sci. 4 (6) (2011) 1946–1971.

[15] D. Qin, et al., Three-dimensional architecture constructed from a graphene oxide nanosheet–polymer composite for high-flux forward osmosis membranes, J. Mater. Chem. A 5 (24) (2017) 12183–12192.

[16] S. Castelletto, A. Boretti, Advantages, limitations, and future suggestions in studying graphene-based desalination membranes, RSC Adv. 11 (14) (2021) 7981–8002.

[17] D.J. Johnson, N. Hilal, Can graphene and graphene oxide materials revolutionise desalination processes? Desalination 500 (2020) 114852.

[18] F. Yan, et al., Preparation of freestanding graphene-based laminar membrane for clean-water intake via forward osmosis process, RSC Adv. 7 (3) (2017) 1326–1335.

[19] A. Ali, et al., Laminar graphene oxide membranes towards selective ionic and molecular separations: challenges and progress, Chem. Rec. 20 (4) (2020) 344–354.

[20] X. Fan, Y. Liu, X. Quan, A novel reduced graphene oxide/carbon nanotube hollow fiber membrane with high forward osmosis performance, Desalination 451 (2019) 117–124.

[21] N.H. Barbhuiya, U. Misra, S.P. Singh, Synthesis, fabrication, and mechanism of action of electrically conductive membranes: a review, Environ. Sci.: Water Res. Technol. 7 (4) (2021) 671–705.

[22] L.G. Guex, et al., Experimental review: chemical reduction of graphene oxide (GO) to reduced graphene oxide (rGO) by aqueous chemistry, Nanoscale 9 (27) (2017) 9562–9571.

[23] S. Rao, et al., Reduced graphene oxide: effect of reduction on electrical conductivity, J. Compos. Sci. 2 (2) (2018) 25.

[24] V.B. Mohan, et al., Characterisation of reduced graphene oxide: effects of reduction variables on electrical conductivity, Mater. Sci. Eng. B 193 (2015) 49–60.

[25] A. Ronen, S.L. Walker, D. Jassby, Electroconductive and electroresponsive membranes for water treatment, Rev. Chem. Eng. 32 (5) (2016) 533–550.

[26] H. Liu, et al., In situ synthesis of the reduced graphene oxide–polyethyleneimine composite and its gas barrier properties, J. Mater. Chem. A 1 (11) (2013) 3739–3746.

[27] B. Li, et al., One-step electrochemically prepared graphene/polyaniline conductive filter membrane for permeation enhancement by fouling mitigation, Langmuir 36 (9) (2020) 2209–2222.

[28] Z. Zhang, et al., Electrically conductive inorganic membranes: a review on principles, characteristics and applications, Chem. Eng. J. 427 (2022) 131987.

[29] M. Reyes-Reyes, I. Cruz-Cruz, R. López-Sandoval, Enhancement of the electrical conductivity in PEDOT: PSS films by the addition of dimethyl sulfate, J. Phys. Chem. C 114 (47) (2010) 20220–20224.

[30] A.N. Reshetilov, et al., Highly conductive polymer PEDOT: PSS—application in biomedical and bioelectrochemical systems, RENSIT 12 (2020) 471–482.

[31] S. Sarkar, et al., Structural and electrical behaviours of PEDOT: PSS thin films in presence of negatively charged gold and silver nanoparticles: a green synthesis approach, Synth. Met. 279 (2021) 116848.

[32] G.E. Fenoy, et al., Functionalization strategies of PEDOT and PEDOT: PSS films for organic bioelectronics applications, Chemosensors 9 (8) (2021) 212.

[33] N. Gholampour, D. Brian, M. Eslamian, Tailoring characteristics of PEDOT: PSS coated on glass and plastics by ultrasonic substrate vibration post treatment, Coatings 8 (10) (2018) 337.

[34] A. Pasha, S. Khasim, RETRACTED ARTICLE: highly conductive organic thin films of PEDOT–PSS: silver nanocomposite treated with PEG as a promising thermo-electric material, J. Mater. Sci. Mater. Electron. 31 (12) (2020) 9185–9195.

[35] N. Massonnet, et al., Improvement of the Seebeck coefficient of PEDOT: PSS by chemical reduction combined with a novel method for its transfer using free-standing thin films, J. Mater. Chem. C 2 (7) (2014) 1278–1283.

[36] J. Park, et al., Electrical and thermal properties of PEDOT: PSS films doped with carbon nanotubes, Synth. Met. 161 (5–6) (2011) 523–527.

[37] N. Chakraborty, et al., PEDOT: PSS-doped graphene oxide as an alternative to hole transport material and transparent conducting electrode, Nano 17 (14) (2022) 2250115.

[38] G.J. Adekoya, R.E. Sadiku, S.S. Ray, Nanocomposites of PEDOT: PSS with graphene and its derivatives for flexible electronic applications: a review, Macromol. Mater. Eng. 306 (3) (2021) 2000716.

[39] P.S. Goh, et al., Recent progresses of forward osmosis membranes formulation and design for wastewater treatment, Water 11 (10) (2019) 2043.

[40] M. Rastgar, et al., Substantially improved antifouling properties in electro-oxidative graphene laminate forward osmosis membrane, Chem. Eng. Res. Des. 141 (2019) 413–424.

[41] Y. Li, et al., Antifouling conductive composite membrane with reversible wettability for wastewater treatment, Membranes 12 (6) (2022) 626.

[42] Q. Liu, et al., An effective design of electrically conducting thin-film composite (TFC) membranes for bio and organic fouling control in forward osmosis (FO), Environ. Sci. Technol. 50 (19) (2016) 10596–10605.

[43] S. Morales-Torres, et al., Thin-film composite forward osmosis membranes based on polysulfone supports blended with nanostructured carbon materials, J. Membr. Sci. 520 (2016) 326–336.

[44] J. Jang, et al., Graphene oxide nanocomposite membrane cooperatively cross-linked by monomer and polymer overcoming the trade-off between flux and rejection in forward osmosis, J. Membr. Sci. 598 (2020) 117684.

[45] A. Saeedi-Jurkuyeh, et al., A novel synthetic thin-film nanocomposite forward osmosis membrane modified by graphene oxide and polyethylene glycol for heavy metals removal from aqueous solutions, React. Funct. Polym. 146 (2020) 104397.

[46] P. Deka, et al., Performance evaluation of reduced graphene oxide membrane doped with polystyrene sulfonic acid for forward osmosis process, Sustain. Energy Technol. Assess. 44 (2021) 101093.

[47] Q. She, et al., Membrane fouling in osmotically driven membrane processes: a review, J. Membr. Sci. 499 (2016) 201–233.

[48] N. Padmavathy, et al., Interlocked graphene oxide provides narrow channels for effective water desalination through forward osmosis, ACS Appl. Mater. Interfaces 11 (7) (2019) 7566–7575.

[49] C. Li, et al., Flexible graphene electrothermal films made from electrochemically exfoliated graphite, J. Mater. Sci. 51 (2016) 1043–1051.

[50] J. Lu, et al., One-pot synthesis of fluorescent carbon nanoribbons, nanoparticles, and graphene by the exfoliation of graphite in ionic liquids, ACS Nano 3 (8) (2009) 2367–2375.

[51] Y. Zhang, S. Zhang, T.-S. Chung, Nanometric graphene oxide framework membranes with enhanced heavy metal removal via nanofiltration, Environ. Sci. Technol. 49 (16) (2015) 10235–10242.

[52] P. Leroy, C. Tournassat, M. Bizi, Influence of surface conductivity on the apparent zeta potential of TiO2 nanoparticles, J. Colloid Interface Sci. 356 (2) (2011) 442–453.

[53] M. Al-Furaiji, et al., Preparation of thin-film composite membranes supported with electrospun nanofibers for desalination by forward osmosis, Drink Water Eng. Sci. 13 (2) (2020) 51–57.

[54] S. Kim, et al., Highly crosslinked, chlorine tolerant polymer network entwined graphene oxide membrane for water desalination, J. Mater. Chem. A 5 (4) (2017) 1533–1540.

[55] J.H. Jhaveri, Z. Murthy, A comprehensive review on anti-fouling nanocomposite membranes for pressure driven membrane separation processes, Desalination 379 (2016) 137–154.

[56] Z. Zhu, et al., Photopatternable PEDOT: PSS/PEG hybrid thin film with moisture stability and sensitivity, Microsyst. Nanoeng. 3 (1) (2017) 1–9.

[57] S. Ghosh, et al., Fabrication and investigation of 3D tuned PEG/PEDOT: PSS treated conductive and durable cotton fabric for superior electrical conductivity and flexible electromagnetic interference shielding, Compos. Sci. Technol. 181 (2019) 107682.

[58] Z.-Y. Sui, et al., Preparation of three-dimensional graphene oxide–polyethylenimine porous materials as dye and gas adsorbents, ACS Appl. Mater. Interfaces 5 (18) (2013) 9172–9179.

[59] X. Zhou, et al., The carbonization of polyethyleneimine: facile fabrication of N-doped graphene oxide and graphene quantum dots, RSC Adv. 5 (128) (2015) 105855–105861.

[60] P. Li, et al., Preparation of modified graphene oxide/polyethyleneimine film with enhanced hydrogen barrier properties by reactive layer-by-layer self-assembly, Compos. B Eng. 166 (2019) 663–672.

[61] P.S. Parsamehr, et al., Preparation of novel cross-linked graphene oxide membrane for desalination applications using (EDC and NHS)-activated graphene oxide and PEI, Desalination 468 (2019) 114079.

[62] N.B. Darwish, et al., Effect of lithium chloride additive on forward osmosis membranes performance, J. Water Process Eng. 33 (2020) 101049.

[63] R. Kumar, M. Mamlouk, K. Scott, Sulfonated polyether ether ketone–sulfonated graphene oxide composite membranes for polymer electrolyte fuel cells, RSC Adv. 4 (2) (2014) 617–623.

[64] S. Ayyaru, Y.-H. Ahn, Application of sulfonic acid group functionalized graphene oxide to improve hydrophilicity, permeability, and antifouling of PVDF nanocomposite ultrafiltration membranes, J. Membr. Sci. 525 (2017) 210–219.

[65] D.A. Mengistie, P.-C. Wang, C.-W. Chu, Effect of molecular weight of additives on the conductivity of PEDOT: PSS and efficiency for ITO-free organic solar cells, J. Mater. Chem. A 1 (34) (2013) 9907–9915.

[66] E. Susanti, P. Wulandari, Effect of localized surface plasmon resonance from incorporated gold nanoparticles in PEDOT: PSS hole transport layer for hybrid solar cell applications, in: Journal of Physics: Conference Series, IOP Publishing, 2018.

[67] M. Edokali, et al., Chemical modification of reduced graphene oxide membranes: enhanced desalination performance and structural properties for forward osmosis, Chem. Eng. Res. Des. 199 (2023) 659–675.

[68] U. Lang, et al., Microscopical investigations of PEDOT: PSS thin films, Adv. Funct. Mater. 19 (8) (2009) 1215–1220.

[69] A.M. Díez-Pascual, A.L. Díez-Vicente, Poly (propylene fumarate)/polyethylene glycol-modified graphene oxide nanocomposites for tissue engineering, ACS Appl. Mater. Interfaces 8 (28) (2016) 17902–17914.

[70] L.-S. Tang, et al., Polyethylene glycol/graphene oxide aerogel shape-stabilized phase change materials for photo-to-thermal energy conversion and storage via

tuning the oxidation degree of graphene oxide, Energy Convers. Manag. 146 (2017) 253–264.

[71] M. Niu, et al., Polyethylene glycol grafted with carboxylated graphene oxide as a novel interface modifier for polylactic acid/graphene nanocomposites, R. Soc. Open Sci. 7 (7) (2020) 192154.

[72] D. Alemu, et al., Highly conductive PEDOT: PSS electrode by simple film treatment with methanol for ITO-free polymer solar cells, Energy Environ. Sci. 5 (11) (2012) 9662–9671.

[73] A.A. Farah, et al., Conductivity enhancement of poly (3, 4-ethylenedioxythiophene)-poly (styrenesulfonate) films post-spincasting, J. Appl. Phys. 112 (11) (2012).

[74] W.-S. Kuo, et al., Amino-functionalized nitrogen-doped graphene quantum dots for efficient enhancement of two-photon-excitation photodynamic therapy: functionalized nitrogen as a bactericidal and contrast agent, Int. J. Nanomedicine (2020) 6961–6973.

[75] S.-P. Rwei, et al., Characterization of solvent-treated PEDOT: PSS thin films with enhanced conductivities, Polymers 11 (1) (2019) 134.

[76] X. Wang, et al., Enhancement of thermoelectric performance of PEDOT: PSS films by post-treatment with a superacid, RSC Adv. 8 (33) (2018) 18334–18340.

[77] E. Hosseini, V.O. Kollath, K. Karan, The key mechanism of conductivity in PEDOT: PSS thin films exposed by anomalous conduction behaviour upon solvent-doping and sulfuric acid post-treatment, J. Mater. Chem. C 8 (12) (2020) 3982–3990.

[78] Y. Yuan, et al., Enhanced desalination performance of carboxyl functionalized graphene oxide nanofiltration membranes, Desalination 405 (2017) 29–39.

[79] Y. Zhao, L. Duan, S.W. Hermanowicz, Influence of water transport characteristics on membrane internal conductive structure in forward osmosis microbial fuel cell, J. Mol. Liq. 380 (2023) 121704.

[80] E. Yang, et al., Laminar reduced graphene oxide membrane modified with silver nanoparticle-polydopamine for water/ion separation and biofouling resistance enhancement, Desalination 426 (2018) 21–31.

[81] C.F. Wan, et al., Nanostructured membranes for enhanced forward osmosis and pressure-retarded osmosis, in: Sustainable Nanoscale Engineering, Elsevier, 2020, pp. 373–394.

[82] A. Bogler, S. Lin, E. Bar-Zeev, Biofouling of membrane distillation, forward osmosis and pressure retarded osmosis: principles, impacts and future directions, J. Membr. Sci. 542 (2017) 378–398.

[83] P.-F. Sun, et al., Effects of reverse solute diffusion on membrane biofouling in pressure-retarded osmosis processes, Desalination 512 (2021) 115145.

[84] X. Lu, et al., In situ surface chemical modification of thin-film composite forward osmosis membranes for enhanced organic fouling resistance, Environ. Sci. Technol. 47 (21) (2013) 12219–12228.

[85] H. Salehi, M. Rastgar, A. Shakeri, Anti-fouling and high water permeable forward osmosis membrane fabricated via layer by layer assembly of chitosan/graphene oxide, Appl. Surf. Sci. 413 (2017) 99–108.

[86] V. Kochkodan, D.J. Johnson, N. Hilal, Polymeric membranes: surface modification for minimizing (bio) colloidal fouling, Adv. Colloid Interf. Sci. 206 (2014) 116–140.

[87] T. Sunohara, T. Masuda, Cellulose triacetate as a high-performance membrane, High-performance Membrane Dialyzers 173 (2011) 156–163.

[88] Herron, J., *Asymmetric forward osmosis membranes*. 2008, US Patent US7,445,712.

[89] B. Mi, M. Elimelech, Chemical and physical aspects of organic fouling of forward osmosis membranes, J. Membr. Sci. 320 (1–2) (2008) 292–302.

[90] Y.-N. Wang, C.Y. Tang, Fouling of nanofiltration, reverse osmosis, and ultrafiltration membranes by protein mixtures: the role of inter-foulant-species interaction, Environ. Sci. Technol. 45 (15) (2011) 6373–6379.

[91] A. Ilyas, et al., Micro-patterned cellulose triacetate membranes for forward osmosis: synthesis, performance and anti-fouling behavior, Desalination 542 (2022) 116076.

[92] M.B.M.Y. Ang, et al., Merits of using cellulose triacetate as a substrate in producing thin-film composite nanofiltration polyamide membranes with ultra-high performance, J. Taiwan Inst. Chem. Eng. 112 (2020) 251–258.

[93] R.C. Ong, T.-S. Chung, Fabrication and positron annihilation spectroscopy (PAS) characterization of cellulose triacetate membranes for forward osmosis, J. Membr. Sci. 394 (2012) 230–240.

[94] H.-R. Chae, et al., Graphene oxide-embedded thin-film composite reverse osmosis membrane with high flux, anti-biofouling, and chlorine resistance, J. Membr. Sci. 483 (2015) 128–135.

[95] Z. Li, et al., Graphene oxide incorporated forward osmosis membranes with enhanced desalination performance and chlorine resistance, Front. Chem. (2019) 7.

[96] H. Kang, et al., Interlamination restrictive effect of carbon nanotubes for graphene oxide forward osmosis membrane via layer by layer assembly, Appl. Surf. Sci. 465 (2019) 1103–1106.

[97] M. Hu, S. Zheng, B. Mi, Organic fouling of graphene oxide membranes and its implications for membrane fouling control in engineered osmosis, Environ. Sci. Technol. 50 (2) (2016) 685–693.

[98] H. Liu, H. Wang, X. Zhang, Facile fabrication of freestanding ultrathin reduced graphene oxide membranes for water purification, Adv. Mater. 27 (2) (2015) 249–254.

[99] M. Kadhom, B. Deng, Synthesis of high-performance thin film composite (TFC) membranes by controlling the preparation conditions: technical notes, J. Water Process Eng. 30 (2019) 100542.

[100] H.L.a.W. Yang, in: H.-Y. Jeon (Ed.), Electrospinning Technology in Non-woven Fabric Manufacturing, Electrospinning Technology in Non-woven Fabric Manufacturing, IntechOpen Science, 2016, p. 326.